Tectonics

RESEARCH ARTICLE
10.1029/2018TC005175

Special Section:
The 2016 Central Italy Seismic Sequence: Insights, implications and lessons learned

Surface Faulting of the 30 October 2016 M_w 6.5 Central Italy Earthquake: Detailed Analysis of a Complex Coseismic Rupture

F. Villani[1], S. Pucci[1], R. Civico[1], P. M. De Martini[1], F. R. Cinti[1], and D. Pantosti[1]

[1]Istituto Nazionale di Geofisica e Vulcanologia, Rome, Italy

Key Points:
- We analyze the surface ruptures of the 30 October 2016 M_w 6.5 Norcia normal-faulting earthquake in central Italy
- The heterogeneity of surface slip, with peaks up to 2.10 m, is controlled by the coseismic rupture process at depth
- The scaling properties and the complexity of surface slip reveal processes of fault segmentation and strain localization

Supporting Information:
- Supporting Information S1
- Table S1

Correspondence to:
F. Villani,
fabio.villani@ingv.it

Citation:
Villani, F., Pucci, S., Civico, R., De Martini, P. M., Cinti, F. R., & Pantosti, D. (2018). Surface faulting of the 30 October 2016 M_w 6.5 central Italy earthquake: Detailed analysis of a complex coseismic rupture. *Tectonics*, *37*, 3378–3410. https://doi.org/10.1029/2018TC005175

Received 11 JUN 2018
Accepted 31 AUG 2018
Accepted article online 4 SEP 2018
Published online 2 OCT 2018

Abstract The study of coseismic surface ruptures provides insights into earthquakes dynamics and fault growth processes. We analyze the surface faulting related to the seismic sequence that hit central Italy in 2016–2017, focusing on the ruptures caused by 30 October 2016 M_w 6.5 Norcia earthquake. They are located on the NW trending normal fault splays of the Mount Vettore-Mount Bove fault system (VBFS), forming a fracture network made of hundreds of strands striking N135–160°. The surface rupture length for this event is ~22 km, with average surface slip of ~0.44 m and peak of ~2.10 m. The collected coseismic slip vectors yield an average N233° trending extension, consistent with the local structural setting and seismological data. Surface slip displays cumulative frequency-size distributions of rupture length and offset that follow power law and exponential scaling over 2 orders of magnitude, respectively. We observe strain localization on a few major fault splays of the VBFS, causing a markedly asymmetric along-strike slip profile, with a high gradient to the southeast. The ~5-km-long Cordone del Vettore fault accounts for 40% of the overall coseismic surface slip. We infer that the heterogeneous slip at depth, coupled with the highly segmented nature of the VBFS and its interference with thrusts and adjacent active normal faults, has control over the pattern of surface faulting. For the Norcia earthquake, a robust scaling of surface slip area with rupture length accounts for extreme slip peaks over relatively short ruptures, which we envisage may be typical of the VBFS long-term growth.

1. Introduction

Surface-rupturing earthquakes represent a unique opportunity to investigate the impact of coseismic faulting on landscape evolution and to refine models of brittle deformation affecting the upper crust (Burbank & Anderson, 2011; Bull, 2009; Wallace, 1977; Yeats et al., 1997).

Faults grow through the accumulation of seismic slip (Cowie & Scholz, 1992a, 1992b; King et al., 1988; Walsh & Watterson, 1987). The amount and spatial distribution of fault slip depends on several factors, such as fault geometric complexity and segmentation, heterogeneity of stress conditions and rock stiffness, and interaction with adjacent faults (Bruhn & Schultz, 1996; Bürgmann et al., 1994; Scholz, 2002). Repeated earthquakes over several seismic cycles (10^3- to 10^5-year timescales) guide the evolution of fault systems. Incremental fault growth and lateral tip propagation resulting from cumulative single-slip episodes, coupled with stress-induced interactions between nearby faults, promote linkage of smaller segments into larger ones. Many theoretical and field studies suggest that the evolution of complex fault systems entails a progressive hierarchical organization, provided boundary conditions remain stationary during fault nucleation. This results in the development of a few main large faults that accumulate most of the deformation (strain localization), while other faults are eventually deactivated (Ackermann & Schlische, 1997; Cowie, 1998; Cowie et al., 1995; Cowie & Shipton, 1998; Dawers & Anders, 1995; Gupta & Scholz, 2000; Meyer et al., 2002; Nixon et al., 2014; Peacock & Sanderson, 1991). Whether strain localization is achieved at the very beginning of fault network growth or in a more mature stage is matter of debate (Childs et al., 2017; Nicol et al., 2017). However, compelling experimental and outcrop evidence shows that this fundamental process takes place over a wide range of spatial wavelengths, from the structural pattern of kilometer-scale fault systems down to the internal architecture of fault zones (Ben-Zion & Sammis, 2003; Shipton et al., 2006; Wibberley et al., 2008; Yamashita, 2009).

A critical step in seismic hazard assessments is the recognition of structural and geometric complexities within fault systems that hamper rupture propagation (barriers) or, conversely, may favor interaction of adjacent faults on different timescales (D'Alessio & Martel, 2004; Manighetti et al., 2009; Sibson, 1988; Wibberley

et al., 2008). Ultimately, such knowledge yields the basis for establishing the segmented and interacting framework of seismogenic fault systems, with the chance to identify possible recurrent styles of coseismic faulting, potential rupture length, and organization (e.g., DuRoss et al., 2016; Machette et al., 1991). Therefore, the detailed analysis of coseismic surface ruptures may provide precious hints on active faults segmentation and the way they accumulate displacement and grow through time (Lin, 2009).

The trace of coseismic ruptures and the morphology of fault scarps caused by moderate to large earthquakes typically displays geometrical complexity (Anderson, 1951; Choi et al., 2012; Segall & Pollard, 1980; Sibson, 1988; Tchalenko & Berberian, 1975; Vedder & Wallace, 1973) that may attain an extreme degree, as documented in some cases of multifault ruptures involving a very large number of segments (Hamling et al., 2017; Litchfield et al., 2018).

Surface ruptures along normal faults usually appear in map quite irregular: one main reason is that the surface trace develops perpendicularly to the mean slip vector, that is, a direction where fault plane roughness is generally higher (Sagy et al., 2007; Scholz, 2002). Furthermore, normal fault ruptures are complex since they often involve several adjacent segments with large steps (Biasi & Wesnousky, 2016) and multiple splays that concentrate in the hanging wall of the principal deformation zone: this results in an asymmetric across-fault rupture distribution, mostly due to the different stress conditions acting in the footwall and hanging wall blocks during fault propagation (Berg & Skar, 2005).

Seismological and geological analysis of surface-rupturing normal-faulting earthquakes in continental environments shows that they may occur as multiple shocks on different fault segments, resulting in compound surface ruptures. Illustrative case studies are the 1959 M_s7.5 Hebgen Lake earthquake in Montana (Doser, 1985; Wallace, 1980; Witkind et al., 1962), the 1981 M_s 6.7 Corinth earthquake in Greece (Collier et al., 1998; Jackson et al., 1982; King et al., 1985; Roberts, 1996), and the 1983 M_s 7.3 Borah Peak earthquake in Idaho (Bruhn et al., 1987; Crone et al., 1987; Wallace, 1984). Those ruptures display slip partitioning on different strands with variable geometry, and asymmetric along-strike throw distribution, pointing out a link between earthquake source complexity and pattern of surface faulting (Manighetti et al., 2005).

Although several normal-faulting earthquakes ruptured the surface in the last century (see a review in Boncio et al., 2012), detailed quantitative data on the geometric and structural properties of those surface breaks are available only for the most recent events and are relatively few with respect to strike-slip and reverse-type cases (e.g., Stirling et al., 2013; Wesnousky, 2008).

The Apennines (Italy) represent one of the regions with the highest seismogenic potential in the Mediterranean area, mostly due to shallow crustal normal-faulting earthquakes (Amato et al., 1997; Anderson & Jackson, 1987; Chiarabba et al., 2005). In this area, the largest seismic events occur with centennial to millennial recurrence times, so that only a few cases of surface faulting have been studied with a modern scientific approach. Among these, the surface ruptures produced by the 1915 M_w 6.8 Avezzano earthquake in central Italy were reconstructed based on historical reports and subsequent investigations (Galadini & Galli, 1999; Michetti et al., 1996; Oddone, 1915). However, the first well-documented surface rupture dates back to the 23 November 1980 M_w 6.9 Irpinia earthquake in southern Italy. It was a complex earthquake characterized by multiple shocks on different fault segments (Bernard & Zollo, 1989; Cocco et al., 1999; Westaway & Jackson, 1987). Westaway and Jackson (1984) and Pantosti and Valensise (1990) mapped in detail the surface rupture, and subsequent trench investigation by Pantosti et al. (1993) led to the recognition of recurrent Holocene surface faulting along the 1980 earthquake fault, initiating paleoseismology in Italy (Galli et al., 2008).

More recently, detailed studies revealed the occurrence of surface ruptures also in the case of moderate-sized normal-faulting earthquakes in the central Apennines. This was the case of the M_w 6.0, 1997 Colfiorito earthquake (Cello et al., 1997; Cinti et al., 1999; Mildon et al., 2016; Pantosti et al., 1999) and of the M_w 6.1, 2009 L'Aquila earthquake (among the others Boncio et al., 2010; Cinti et al., 2011; EMERGEO Working Group, 2010; Vittori et al., 2011).

The latest event, the 30 October 2016 M_w 6.5 Norcia earthquake (Figure 1), is of paramount importance in the list of recent Italian surface-rupturing earthquakes, because it was the strongest Italian earthquake since the 1980 Irpinia event and produced an impressive complex system of surface ruptures, affecting a > 400 km^2-wide mountainous area. The seismological and geodetic data point out a remarkable complexity of the

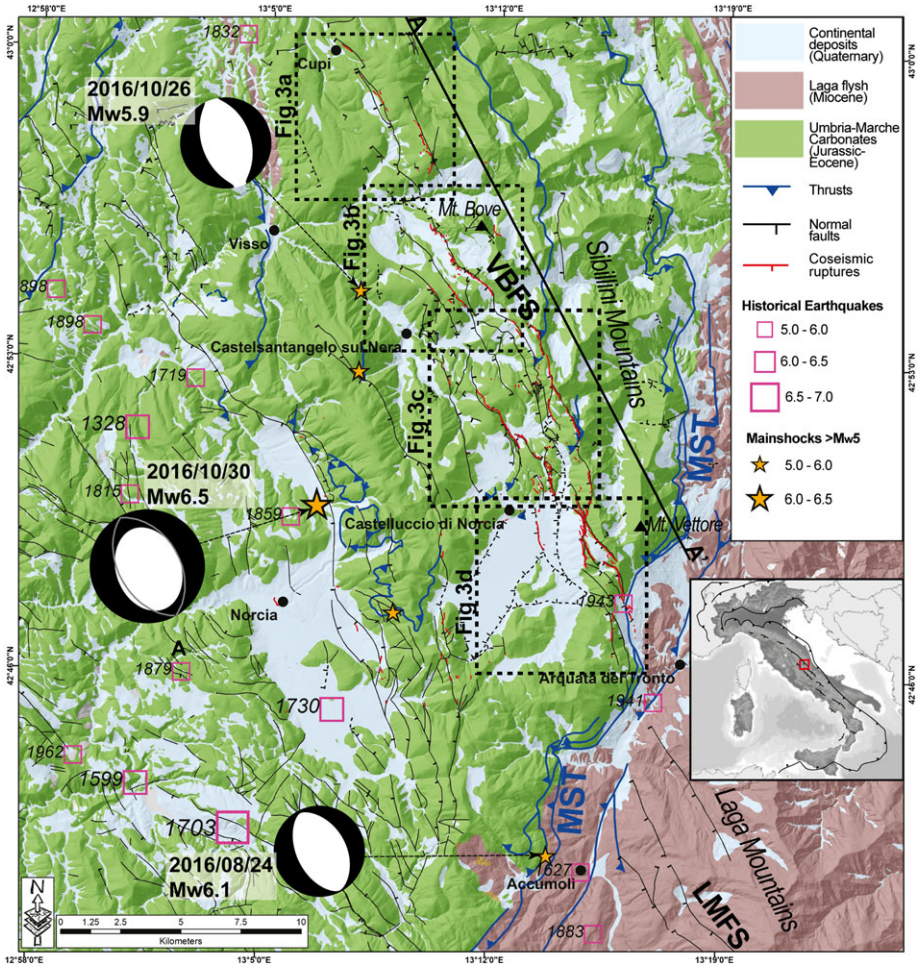

Figure 1. Simplified structural map of the area struck by the 2016–2017 seismic sequence (compiled from 1:10,000-scale cartography of Regione Umbria and Marche, Centamore et al., 1992, and Pierantoni et al., 2013). The labels VBFS and LMFS indicate the Mount Vettore-Mount Bove and Laga Mountains fault systems, respectively. MST indicates the Sibillini Mountains thrust. The pink open squares indicate the main historical seismic events (Rovida et al., 2016). The time-domain moment tensor solutions for the three mainshocks of 24 August, 26 October, and 30 October 2016 are from Tinti et al. (2016), Chiaraluce et al. (2017), and Scognamiglio et al. (2018), respectively. The simplified trace of the coseismic surface ruptures produced by the three mainshocks (in red) is from Civico et al., 2018. A–A′ is the trace of the baseline used for the projection of coseismic surface offset data.

coseismic rupture process (details in section 2), which clearly reflect on the pattern of surface faulting. All this motivates the development of our detailed study on the coseismic ruptures produced by the Norcia earthquake and their relations with the local geology and geomorphology, as they represent a unique opportunity to understand and how to decipher segmentation and potential surface faulting scenarios in these regions.

In this paper, we report a quantitative analysis of the surface ruptures based on the calculation of surface slip distribution, and the description of its geometrical and statistical properties. We take into account the detailed documentation provided by Civico et al. (2018) and Villani et al. (2018) and expand those two works, by focusing on the following: (1) the geometric arrangement of the surface ruptures, (2) the associated surface slip and kinematics, (3) the overall length of the activated fault traces, (4) the rupture segmentation in relation to the known active structures and those produced by past deformation events, and (5) the possible relationships between the surface slip pattern and the complexity of the rupture process at depth. Finally, we elaborate some conceptual understandings regarding normal fault growth, segmentation, and the scaling relationships between seismic moment and surface ruptures in the framework of global empirical scaling laws for dip-slip earthquakes.

2. Geological Background and Seismotectonic Framework

The axial zone of the central Apennines (Italy) is made of Meso-Cenozoic carbonate and siliciclastic rocks that experienced NE thrusting during Miocene–Pliocene times (Vai & Martini, 2001). The Sibillini Mountains thrust (MST; Figure 1) is one of the main resulting compressional structures in this region (Calamita et al., 2012). Since the Late Pliocene–Early Pleistocene, postorogenic extension started affecting the chain (Cavinato & De Celles, 1999; D'Agostino et al., 2001) with the present NE directed extension (Montone et al., 2012) reaching regional rates of 1–2.5 mm/year (D'Agostino et al., 2008, 2011; Devoti et al., 2011). The current extension promotes the release of moderate-sized ($5 < M < 6$) to large (up to M ~7) normal-faulting earthquakes, typically nucleating down to depths of ~15 km (Chiarabba & Chiodini, 2013; Chiarabba et al., 2005; Pondrelli et al., 2006). The catalog of historical earthquakes (complete for $M > 5$ events since ~1300 CE; Rovida et al., 2016) further testifies a high seismogenic potential (Figure 1), since the study area was repeatedly affected by M~6 earthquakes.

The long-term extension originated a compound network of normal fault systems up to ~25–30 km in length, partially coaxial with the Neogene thrusts, mostly NW trending and SW dipping (Figure 1; Barchi et al., 2000; Boncio & Lavecchia, 2000; Cowie & Roberts, 2001; Lavecchia et al., 1994; Roberts et al., 2004). Most of these faults show clear hints of late Pleistocene to recent tectonic activity (offset postglacial deposits and landforms, compound fault scarps affecting both continental deposits and pre-Quaternary bedrock), while geologic and paleoseismic data provide values of individual fault slip rates in the 0.2–1.3 mm/year range (Barchi et al., 2000; Benedetti et al., 2013; Cinti et al., 2018; Cowie et al., 2017; Galadini & Galli, 2000; Galli et al., 2008; Giraudi, 1995).

The study area (Figure 1) encloses two of the easternmost active fault systems in this part of the central Apennines: (1) the Mt. Vettore - Mt. Bove fault-system (VBFS for short; Calamita & Pizzi, 1992, 1994; Calamita et al., 1992; Cello et al., 1997; Pizzi et al., 2002), running ~25 km within the Sibillini Mts. Range; 2) the ~30 km-long Laga Mountains fault-system (hereinafter LMFS; Figure 1; Boncio et al., 2004; Galadini & Galli, 2003). They display a right-stepping relationship with a complex relay zone of distributed deformation crossed by the MST. This region was considered a seismic gap, being bordered by the epicentral areas of recent earthquakes to the west (1979, M_w 5.9 earthquake; Deschamps et al., 1984), to the northwest (1997, Colfiorito sequence; Amato et al., 1998), and to the southeast (2009 L'Aquila seismic sequence; Chiaraluce, 2012). Previous studies pointed out the seismogenic potential of the VBFS and the LMFS (Galadini & Galli, 2003; Boncio et al., 2004), because they are characterized by an apparent lack of significant seismicity (with the exception of the 1639 M 6.3 earthquake that severely affected Amatrice) and by concurrent geomorphic (Calamita et al., 1992; Calamita & Pizzi, 1994; Galadini & Galli, 2000; Lavecchia et al., 1994) and paleoseismic (Galadini & Galli, 2003) evidence of recent activity.

The VBFS and LMFS ruptured in 2016 giving rise to a long seismic sequence (Chiaraluce et al., 2017; Mildon et al., 2017), which began on 24 August 2016 with a M_w 6.1 earthquake located to the NW of Amatrice (close to Accumoli, at 8-km depth), causing 299 fatalities and widespread damage (Figure 1). This earthquake showed a remarkable complexity of the rupture process, which involved the northernmost part of the LMFS and the southernmost part of the VBFS, giving rise to two distinct main slip patches (Tinti et al., 2016). Later on, two shocks occurred in the northernmost part of the VBFS on 26 October close to Visso (M_w 5.6 and M_w 5.9). The M_w 5.9 event (hereinafter Visso earthquake) showed seismological evidence of rupture complexity as well (Chiaraluce et al., 2017). Finally, the largest shock occurred on 30 October close to Norcia (M_w 6.5). The latter, with peak slip values up to ~3 m retrieved from strong motion (Chiaraluce et al., 2017) and Global Positioning System (GPS) data inversion (Cheloni et al., 2017), broke an asperity that had already slipped on 24 August. According to Scognamiglio et al. (2018), the time-domain moment tensor solution for this earthquake has nodal planes trending N151° and N330° with almost pure dip slip, respectively (providing a T axis trending N241°); moreover, the rupture process is highly complex, and it involved most of the VBFS together with a small portion of the MST (further details in section 5.2). Walters et al. (2018) using geodetic data propose an even more complex multifault rupture, involving a larger number of segments, including antithetic and transverse structures.

The Amatrice earthquake produced surface faulting for a minimal length of ~5–6 km along the southernmost part of the VBFS, with average vertical offset of ~0.10–0.15 m and local peaks >0.30 m (EMERGEO Working Group, 2016; Lavecchia et al., 2016; Livio et al., 2016; Pucci et al., 2017). The Visso earthquake caused surface faulting in the northernmost part of the VBFS (EMERGEO Working Group, 2017; Pizzi et al., 2017). However, data

on this event are less abundant, due to the very short time available for surveys before the occurrence of the M_w 6.5 Norcia earthquake. Surface faulting caused by this last event involved almost the entire length of the VBFS overprinting the ruptures of the Amatrice earthquake and part of the Visso earthquake ruptures. Several geologic surveys resulted in (1) a surface rupture map, drawn by inspecting a selection of ~11,000 oblique-view photos from helicopter flights, verified and integrated with field data (Civico et al., 2018), and (2) an open-access database of surface coseismic effects (Villani et al., 2018). Ferrario and Livio (2018) focus on the role of lithology and structural setting in the pattern of surface faulting. Wilkinson et al. (2017), by using low-cost GPS units located in the footwall and in the hanging wall of some splays of the VBFS, demonstrate that the surface rupture process completed within 6–8 s from the origin time of the mainshock, before the onset of the peak ground acceleration: therefore, they infer that the coseismic surface breaks developed at a rate comparable to the rupture propagation speed, as direct expression of primary surface faulting.

3. Data and Methods

3.1. Surface Rupture Mapping and Field Data Collection

The main data we use in this work are the surface rupture map by Civico et al. (2018) and the database of coseismic effects by Villani et al. (2018): these two papers report full technical details about remote mapping and field data collection. For the purpose of this work, we integrated the database (containing records collected between November 2016 and July 2017), with new unpublished data acquired during field surveys that we carried out on August and September 2017 (Table S1 in the supporting information). In total, we analyze ~5,200 surface offset data points.

Overall, those data provide a pattern of the near-field coseismic displacement and geometric arrangement of the rupture that is adequate at nearly 1:5,000 scale. They include some intrinsic uncertainty in the location, due to the use of hand-held GPS and to inaccuracies in georeferencing and rectifying the oblique-view images (details in Villani et al., 2018).

3.2. Surface Offset Measurements and Analysis

The clear tectonic origin of almost all of the coseismic ruptures is testified by the following features: (1) strict relation with preexisting faults; (2) significant linear extent (tens to hundreds of meters), which is independent of local morphology and bedrock lithology; (3) coherent extensional structural arrangement given by kinematic compatibility of step overs and relays at different scales; (4) consistent kinematics provided by coseismic slip vectors, in accordance with long-term fault striae; and (5) tapering of surface offset at rupture ends and smooth summed throws of overstepping strands. We rejected some measurements that after a careful analysis resulted on shallow slide scars triggered by the earthquake and affecting the scree cover: most of those slides were already mapped by Civico et al. (2018) and display a wide azimuthal dispersion.

Some outcrops show the link of the surface ruptures affecting loose deposits with the underlying causative bedrock fault planes, so their inspection allows us to relate the measurement of some geometric features of the coseismic ruptures to the fault throw and heave, respectively, as vertical and horizontal components of the true slip along the fault plane (Figure 2).

It is known that when the slip on the main fault (dipping ~55–70°) approaches very shallow depths (~1–2 m), it may propagate upward as a high-angle fracture into the loose deposits in the hanging wall. In fact, the dilatant stress conditions close to the free surface favor mode-I (tensile) cracking and hybrid failure (also known as *dilational faulting*, Ferrill & Morris, 2003). Therefore, the free face height is a proxy for fault throw. Accordingly, the horizontal displacement (i.e., opening) equals heave at depth, bearing in mind that the gravitational collapse of the free face may occur, thus causing a small overestimation of the true heave (Figure 2a). This configuration is similar to the *gravity graben* model (Gilbert, 1890), widely adopted by Slemmons (1957) for describing the surface ruptures following the 1954 Dixie Valley earthquake. Sometimes, in presence of thin cover of loose deposits in the hanging wall block, almost all of the slip localizes onto the bedrock fault plane, with a very small amount of opening. In such conditions, the measurement of coseismic net slip is straightforward (Figure 2b). We also observe that, across some overstepping fractures, the relay zone appears breached by a single discrete shear zone, whose net slip equates the summed slip of the overstepping surface ruptures.

The collected measurements are different depending on the type of free face. Along free faces affecting loose soils and debris cover, we measure the maximum local height (vertical offset, *Vo*) and opening (*O*), and,

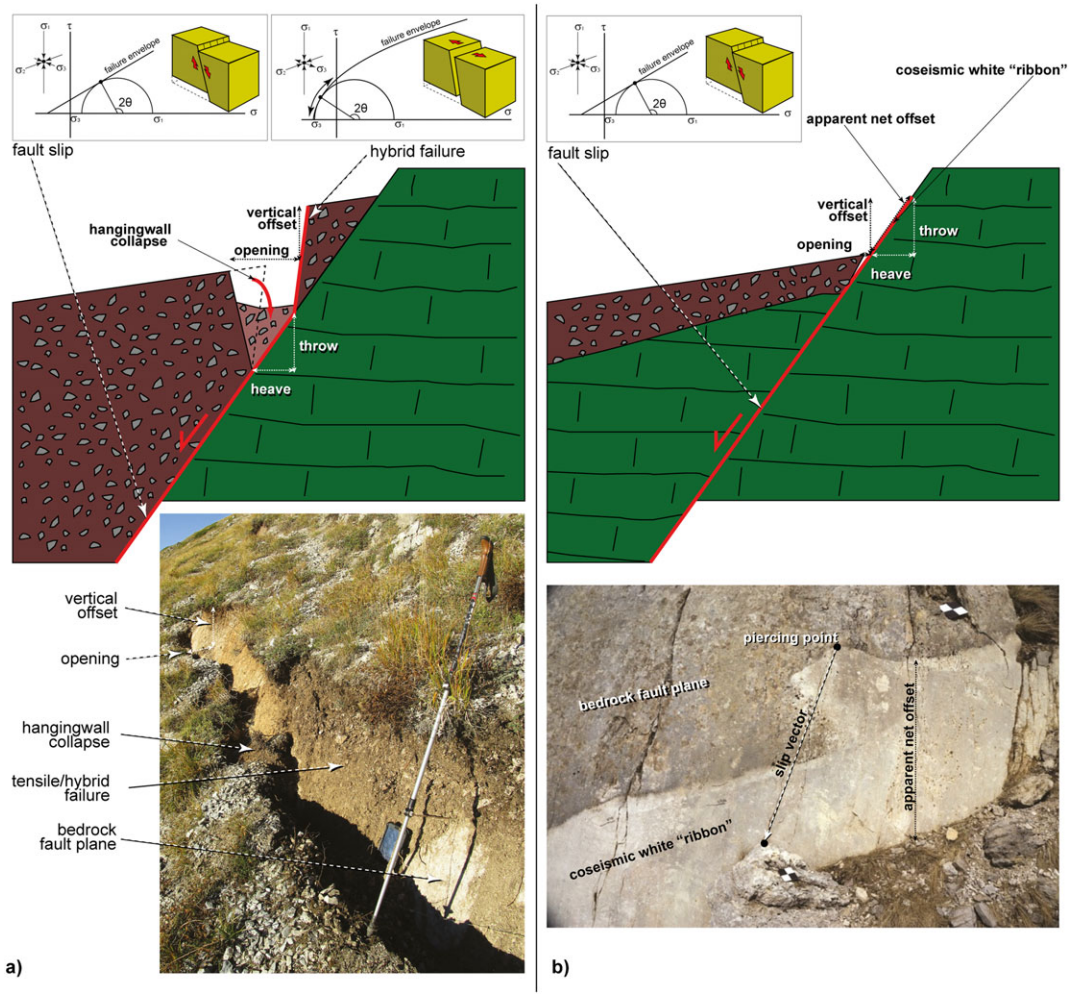

Figure 2. Modified version of the *gravity graben* model (after Slemmons, 1957) applied to the coseismic ruptures analyzed in this paper. (a, bottom) Picture of a coseismic free face on unconsolidated soils covering the bedrock plane and main geometric parameters measured in the field (trekking stick and smartphone for scale). (a, top): Sketch of the tensional field that promotes shear and hybrid failure. (b, bottom left) Picture of coseismic free face on bedrock fault, with the coseismic slip vector defined by clearly recognizable piercing points. (b, upper left) Sketch of the tensional field that promotes shear failure.

whenever possible, the net slip (*S*) using recognizable structural and/or geomorphic piercing points (Figure 2b). Along free faces on bedrock fault planes, we measure the maximum height (vertical offset) of the coseismic ribbon at the base of the scarp and the opening of additional fractures on scree/debris in the hanging wall. We tried to set in the field a nearly constant ~10-m spacing of measurement points; however, in some cases the points are more widely spaced, due to unfavorable local conditions.

The large amount of data collected required a preliminary statistical analysis to cope with the intrinsic heterogeneity of surface faulting and to provide spatially averaged surface slip values so that we can make comparisons with the coseismic slip at depth (inferred from seismological and geodetic data modeling). This first step of analysis is mainly thought to (1) account for the positioning error of data points and uneven spacing, (2) mitigate the dispersion in the distribution of the slip measurements (due to decoupling of the surface loose deposits from the rupturing fault plane), and (3) eliminate possible outliers (due to measurement errors or local nontectonic effects like shallow slide scars).

Following the first analysis, we can describe the magnitude and the statistical properties of surface faulting using frequency histograms of vertical offset and opening, and calculating parameters such as median value, skewness (*skew*), and excess kurtosis (*kurt*). After that, we construct the along-strike median vertical offset and median opening curves for each rupture splay (*Vo-x* and *O-x* curves). To do this, we split the smooth envelope

of the splays into 100-m long fixed windows, in order to include a sufficient number of data points and encompass the average rupture length (see section 4). We use the median instead of the mean and the median absolute deviation (MAD) instead of the standard deviation: they are more appropriate statistical descriptors of our data (section 4.3), because surface slip does not follow a normal distribution (see also Pucci et al., 2017).

In order to explore possible relations between surface offset and local morphology, we compare *Vo-x* and *O-x* curves with absolute elevation and local slope (extracted from a 10-m Digital Elevation Model (DEM), Tarquini et al., 2012; see also Figures S7 to S11 in the supporting information). Then, we combine *Vo-x* and *O-x* curves to obtain throw and heave curves (*T-x* and *H-x*, respectively). Note that *T-x* curves represent *net* throw: in fact, within each window we subtract the contribution of antithetic splays from the summed throws of SW dipping synthetic splays, because in conjugated normal fault sets the antithetic throws are not additive. Finally, we derive the aggregate dip-slip profile of the overall surface rupture (*S-x* curve; see section 5).

The scaling properties of the overall surface rupture are described by comparing average surface slip S_{avg} and rupture length L_s. We also compare the total surface faulting area (SA_{surf}) and L_s, following a similar approach by Scholz et al. (1993). The surface faulting area is a measure of the amount of exposed fault surface due to coseismic slip, thus defining the overall quantity of coseismic fault slip occurred at the surface, and is equal to the integral of the aggregate slip curve *S-x*:

$$SA_{surf} = \int_0^{L_s} S(x)dx$$

A good proxy for SA_{surf} is the product $S_{avg} \times L_s$.

3.3. Kinematic Data Analysis

The kinematic data collected in the field comprise the measurement of rake, trend, and plunge of coseismic slip vectors, mostly consisting of fresh mud smears and subtle striations recording relative motion on bedrock fault planes. In some cases, we can directly measure the attitude and magnitude of slip vectors using footwall and hanging wall piercing points (displaced soil fragments and roots, or bedrock slices; Figure 2b).

To obtain the local extension direction for each subsegment of the rupture, we display a selection of the most representative collected coseismic kinematic indicators. We calculate the trend and plunge of the strain tensor's principal axes, obtained by linked Bingham analysis of coseismic slip vectors (Marrett & Allmendinger, 1990), a statistical procedure based on a geometric method, where the plane containing the slip vector and the normal vector to the fault plane also contains the respective extension and shortening axes, making an angle of 45° with each of the vectors. From a given slip vectors population, all the kinematically consistent extension-shortening pairs are contoured as axial data, and the retrieved directional maxima represent the shortening and extension axes of the incremental strain tensor (*S1* and *S3*, corresponding to the *P* and *T* axes, respectively).

We complement the large-scale deformation map with a plot of averaged slip vectors. For some particular cases, we show how slip rake varies along the strike of the most important activated fault segments, in order to explore the consistency of the retrieved extensional strain field.

4. Results

4.1. Morphology, Geometry, and Structural Pattern of Coseismic Ruptures

Considering the surface ruptures following the Amatrice, Visso, and Norcia earthquakes from the northwesternmost to the southeasternmost tip, they attain a minimum length of ~28 km, parallel to the Sibillini Mountains range (Figures 1 and 3). The ruptures form a complex pattern resulting from the activation of several distinct SW dipping (synthetic) and NE dipping (antithetic) fault splays of the VBFS that for the most part were previously mapped (Calamita & Pizzi, 1992, 1994; Pizzi et al., 2002). For some of these faults, geomorphic, structural, and paleoseismic studies documented evidence of recent activity (among the others Cello et al., 1997; Galadini & Galli, 2003; Lavecchia et al., 1994).

Most of the coseismic ruptures run along VBFS splays that are associated with long-term cumulative fault scarps, tens to hundreds of meters high, and forming prominent NW trending ridges (reaching an absolute

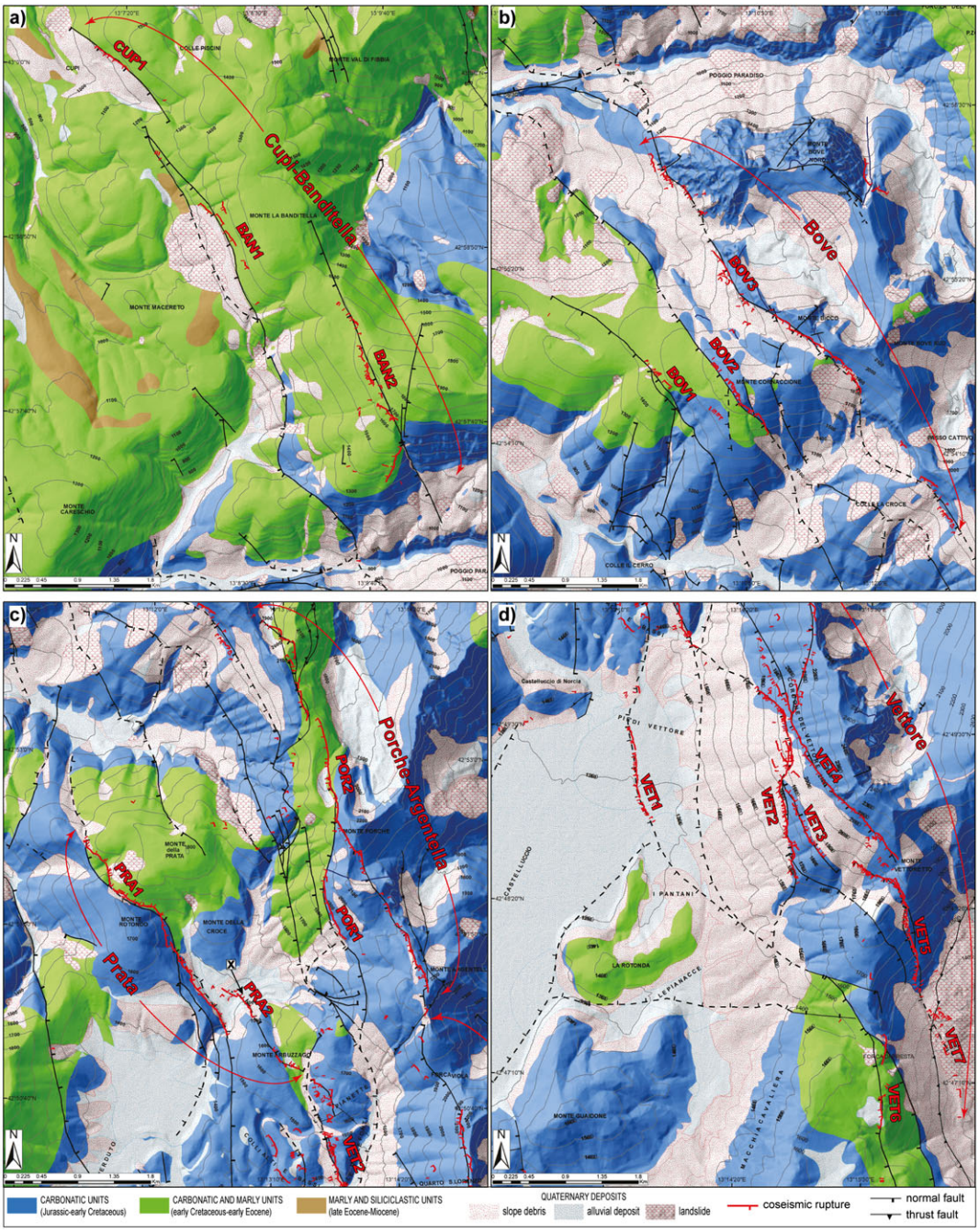

Figure 3. Simplified geological maps of the study area (modified from 1:10,000-scale cartography of Regione Umbria and Marche and Pierantoni et al., 2013), showing the coseismic surface ruptures (in red) subdivided into 5 subsegments comprising 17 main fault splays from NW (top left) to SE (lower right).

elevation of ~2,100–2,400 m a.s.l.). The most important alignment is represented by the Mount Bove-Mount Porche-Mount Argentella-Mount Vettore-Mount Rendentore-Mount Vettoretto ridges, about 12 km in length, with topographic relief locally exceeding 1,100 m. It is bounded almost exclusively by SW dipping normal fault splays (labeled BOV2, BOV3, POR1, POR2, VET1, VET2, VET4, and VET5 in Figure 3). Pizzi and Scisciani (2000) evaluate peak summed geologic throws as large as ~1,200 m for the BOV fault splays, and ~1,350 m for the VET fault splays. Ruptures also affect the base of important E facing cumulative fault scarps related to E dipping normal faults in the Mount Prata area (PRA1 and PRA2 splays in Figure 3), and they run within

the Pian Grande di Castelluccio, the main Quaternary extensional tectonic depression in the Sibillini Mountains (Calamita et al., 1992; Calamita & Pizzi, 1992, 1994; Coltorti & Farabollini, 1995).

In summary, the large-scale pattern of the coseismic surface slip well matches the locus of the long-term cumulative deformation related to the activity of the VBFS, denoting kinematic consistency and suggesting strain localization during the Quaternary.

In order to simplify the description and the analysis of the surface ruptures, in this paper we classify them using the terms rupture strand, rupture splay, and rupture subsegment according to their increasing hierarchical degree. More in detail (1) a *strand* is the shortest identifiable rupture element (typically ~1–50 m in length) mapped in the field and/or recognized through the analysis of oblique-view pictures from helicopter; (2) a *splay* is the envelope of one or more adjacent and/or overlapping strands defining a single normal fault structure at a broader scale (lengths of ~0.5–1 km); (3) a subsegment results from the envelope of one or more kinematically coherent splays defining an independent fault structure over lengths of ~3–7 km and that is clearly separated by adjacent subsegments (due to the occurrence of large underlap or relay zones). We based this classification on (1) the general structural pattern displayed by the rupture, (2) the occurrence of abrupt steps and terminations of the main traces, and (3) the presence of surface offsets and their tapering toward the rupture tips. We group all the recognized strands ($>$ 800) into a subset of 17 fault splays belonging to 5 main subsegments. Such subdivision fairly matches the fault splays of the VBFS that accrued most of the long-term displacement (particularly, splays BOV, POR, and VET).

From the northwest to the southeast, the five main subsegments are (1) Cupi-Banditella (Figure 3a), (2) Bove (Figure 3b), (3) Porche-Argentella (Figure 3c), (4) Prata (Figure 3c), and (5) Vettore (Figure 3d). As a whole, the coseismic ruptures define a complex extensional deformation zone (between the easternmost and the westernmost surface breaks) of variable size, and being on average $<$ 0.5-km wide to the north, ~2.5- to 3.2-km wide in the central part, and ~1-km wide in the southernmost part (see also Figure 14b).

The Cupi-Banditella subsegment (comprising splays CUP1, BAN1, and BAN2 in Figure 3a), is ~7-km long, with average trend of N143°. Our field observations, performed on 28 and 29 October 2016, suggest that this subsegment ruptured during the two 26 October 2016 Visso quakes (M_w 5.6 and M_w 5.9). However, a possible overprinting exerted by the subsequent and larger Norcia earthquake is still a matter of debate, and it cannot be definitely solved due to the insufficient amount of data. Ground breaks are highly discontinuous, and they are organized into three main parallel sets, from NW to SE, being 570-, 1,100-, and 2,500-m long, respectively. The intervening underlap regions are as long as ~800 m. The surface vertical offset displays a median value of 0.15 ± 0.05 m, and a maximum of 0.40 m. The collected kinematic data indicate a pure dip-slip normal motion (the mean rake is −89°) with a local extension direction of N231° (Table 2 and Figure S1 in the supporting information).

The Bove subsegment (comprising splays BOV1, BOV2, and BOV3, in Figure 3b), is ~6-km long and has an average trend of N141°. We did not thoroughly investigate this area as compared to the adjacent sectors, due to safety reasons (area exposed to high landslide hazard). Coseismic surface breaks mapping from helicopter was very useful in this area, although landsliding was hampering a clear inspection of some parts. Our detailed data fully cover only ~2 km of this rupture. An underlap zone of ~1 km separates this subsegment from the SW tip of the Cupi-Banditella one (see Figure 3a for the southern part and Figure 3b for the northern sector). Details of surface offset are in Figure S2 of the supporting information.

The Porche-Argentella and Prata subsegments (respectively, comprising splays POR1, POR2, PRA1, and PRA2 in Figure 3c) represent the central part of the fault system activated during the Norcia earthquake. They include two conjugated faults forming a graben structure. To the east, fault splays POR1 and POR2, are organized in distinct subparallel strands, standing up to 2,100 m a.s.l. along the Sibillini Mountains, with average trends of N155–160° and for a length of ~6 km. The southern termination of the Porche-Argentella subsegment corresponds to a ~600-m long underlap zone that separates it from the adjacent Vettore subsegment. To the west, the ~5-km-long Prata subsegment (comprising the left-stepping fault splays PRA1 and PRA2) is the antithetic counterpart of the Mount Porche faults, characterized by NE dipping splays with average trends of N314–N324°. The *Vo-x* and *O-x* curves (Figure 4b) are quite symmetrical: vertical offset and opening peaks reach ~0.75 and 0.35 m, respectively, at the center (with local maxima of 1 m). Here the envelope of local slope (Figure 4a) is highly heterogeneous and does not evidence any clear relation between surface offset and morphology. Possibly, one exception occurs in the central part, where a relative maximum of local

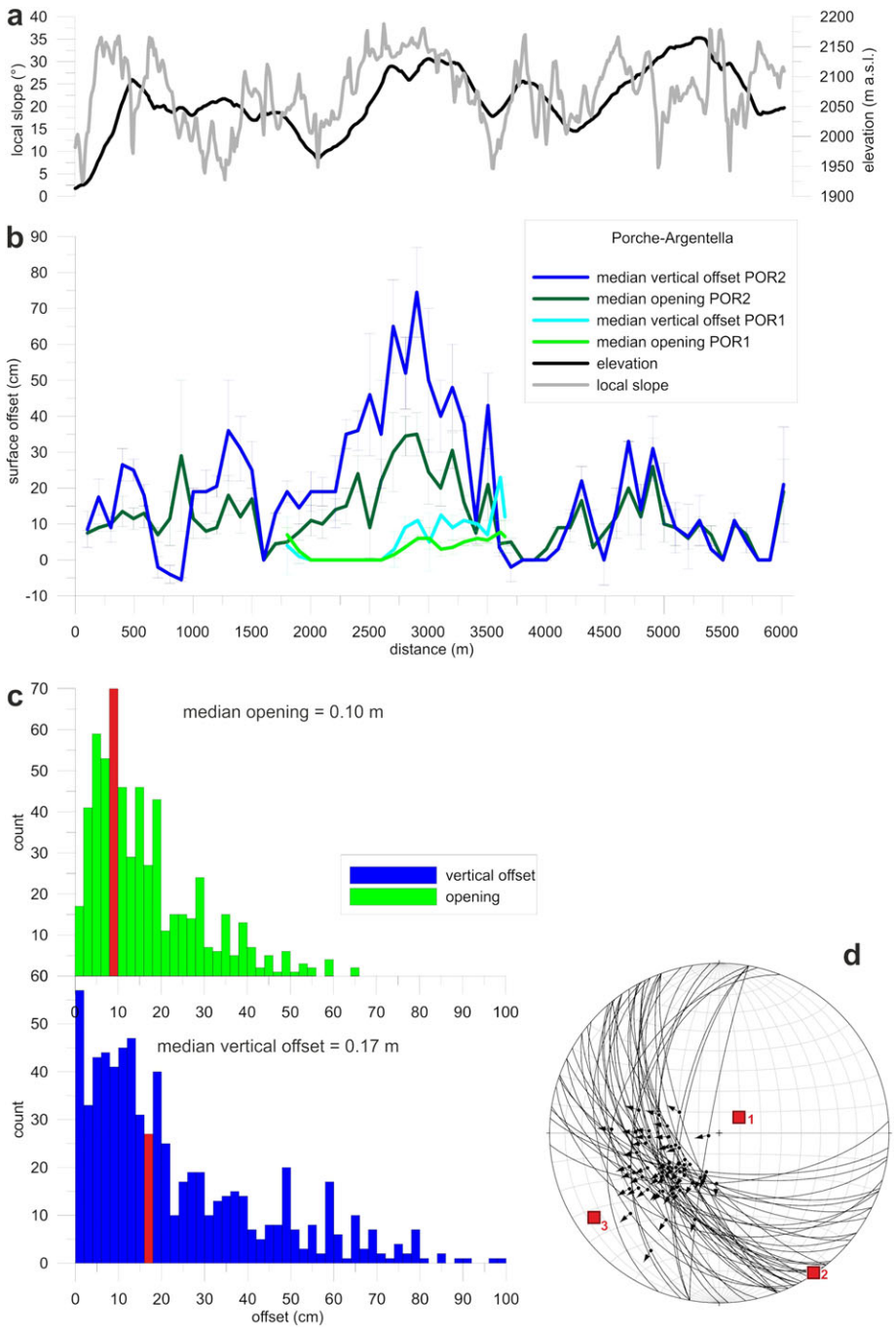

Figure 4. Porche-Argentella subsegment (splays POR1 and POR2). (a) Absolute elevation and local slope along the trace of the coseismic rupture. (b) *Vo-x* and *O-x* curves (error bars = ±1 MAD). (c) Frequency histogram of coseismic ruptures (green: opening; blue: vertical offset), red bars indicate median values. (d) Stereoplot of coseismic slip vectors on bedrock fault planes ($N = 48$). The three kinematic axes are indicated with numbered red squares. See details in the text. MAD = median absolute deviation.

slope (> 30°) roughly matches the region of highest median vertical offset. A ~1.9-km long additional, subparallel alignment of ruptures runs at an average elevation of ~1,900 m a.s.l. on the southwestern slope of Mount Palazzo Borghese (splay POR1). The collected kinematic data (Figure 4d) provide a local extension direction of N236° (Table 2).

On the western part of the graben system, the NE dipping splays PRA1 and PRA2 have a left-stepping relationship and a compound length of ~4,250 m (the overlap is ~600 m and the width of the relay zone is ~400 m). One of the most interesting features observed soon after the Norcia earthquake was a localized ponding related to the coseismic damming of a seasonal stream across the Mount Abuzzago ridge toward the Pian Perduto (indicated with *X* in Figure 3c, EMERGEO Working Group, 2017). The ~3,260-m-long splay PRA1 consists of several smaller strands generally preserving the left-stepping arrangement. It exhibits a markedly asymmetric throw profile, with values increasing to the SE (up to 0.80 m). To the south, the splay PRA2 is ~1,610-m long: there ruptures are discontinuous and a $>$ 450-m-long gap is observed in the central part (Figure 3c). The median vertical offset is 0.11 ± 0.09 m, with a local peak value of 0.51 m that is visible 500 m to the southeast of the northernmost rupture tip. For both splays, surface offset data appear unrelated to local slope and morphology (Figures 5a and 5b). Coseismic slickenlines on bedrock fault planes (Figure 5d and Table 2) show dominant normal dip slip, with a small left-lateral component, on NE dipping planes (average rake: −76°). Data on the few SW dipping ruptures indicate a normal dip-slip motion with a minor right-lateral component. The retrieved extensional axis trends N49°.

The complex Vettore subsegment includes faults of different orientation and dip (corresponding to fault splays VET1, VET2, VET3, VET4, and VET5 in Figure 3d) plus a number of minor related structures (fault splays VET6 and VET7 in Figure 3d). Their average trends range from N150° to N180°. This subsegment is ~9-km long, and, together with the adjacent Bove, Porche-Argentella, and Prata subsegments, it defines a broad extensional zone, up to 2- to 2.5-km wide (Figure 3d). The ruptures affecting the southwestern slope of Mount Redentore-Mount Vettore ridge are by far the most striking, due to the impressive coseismic throw peaks that attracted the scientific community since the early hours of 30 October 2016. The so called *Cordone del Vettore* fault splay (VET4 in Figure 3d), corresponds to a ~5.2-km long, ~20–25-m high, and steep fault scarp cutting through Early Jurassic limestones. Here the rupture runs high on the slope, at an average elevation of 2,080 m a.s.l. (up to 2,224 m a.s.l.; Figure 6a), and it is quite discontinuous in its northernmost 2 km, whereas the southernmost 3 km represent an almost uninterrupted alignment of SW dipping strands. A ~950-m long portion of this splay shows local coseismic slip peaks $>$2 m (Villani et al., 2018): we locally measured up to 2.35-m vertical offset and 2.46-m net slip. Here a bedrock fault scarp with a fresh ribbon is exposed (Figure 7), having average dip of 77° ± 7° and average strike of N144° ± 31° (N = 243).

The median coseismic vertical offset of VET4 is 0.97 ± 0.49 m. The *Vo-x* curve (Figure 6b) is markedly skewed, displaying values $>$1.25 m between 4,000 and 4,750 m along-strike distance and a very sharp gradient, particularly toward the southernmost section tip. The median opening is 0.26 ± 0.14 m, with localized maxima of 1.3 m, which closely follow the regions of highest vertical offset, indicating a positive correlation. Apart from an isolated peak of local slope (65°) matching high median vertical offset (~1.50 m) at ~4,000 m along-strike distance, there seems to be a poor correlation between local slope and coseismic surface offset, highlighting the tectonic origin of ruptures (Figures 6a and S7–S11 in the supporting information). The main reason for this is that the slope along the whole section is very steep ($>$38° on average, higher than along the other investigated splays), due to the long-term cumulative effect of previous surface-rupturing events that created a prominent footwall topography alongside this fault scarp.

Whereas almost all of the other fault splays display right-skewed frequency distributions of vertical offset (Table 1), the Cordone del Vettore splay is characterized by a platykurtic and nearly left-skewed distribution (*kurt* − 0.74), with a modal peak (1.40 m) higher than the median value (Figure 6c).

The analysis of slip vectors (Figure 6d and Table 2) provides a local extension trending N234° (further details in section 4.3).

Another SW facing rupture parallels the Cordone del Vettore fault downslope (splay VET2 in Figure 3d; see also pictures in Figures 7b and 7c), for a total length of ~ 2,900 m. It displays a curved map pattern (diagonal splay, Table 1), transversal to the southwestern slope of Mount Redentore. This rupture follows a subtle fault trace mapped by Calamita et al. (1992, further details in Figure S4 of the supporting information).

A further splay (VET3 in Figure 3d), which was not reported in the official geological maps, ruptured for ~1 km, with NE side down and a counter-slope free face, characterized by local maximum vertical offset of 0.50 m (Figure S3 of the supporting information). The rupture is associated with a subtle topographic break along the southwestern slope of Mount Redentore, suggesting that previous surface-breaking paleo-earthquakes involved also VET3.

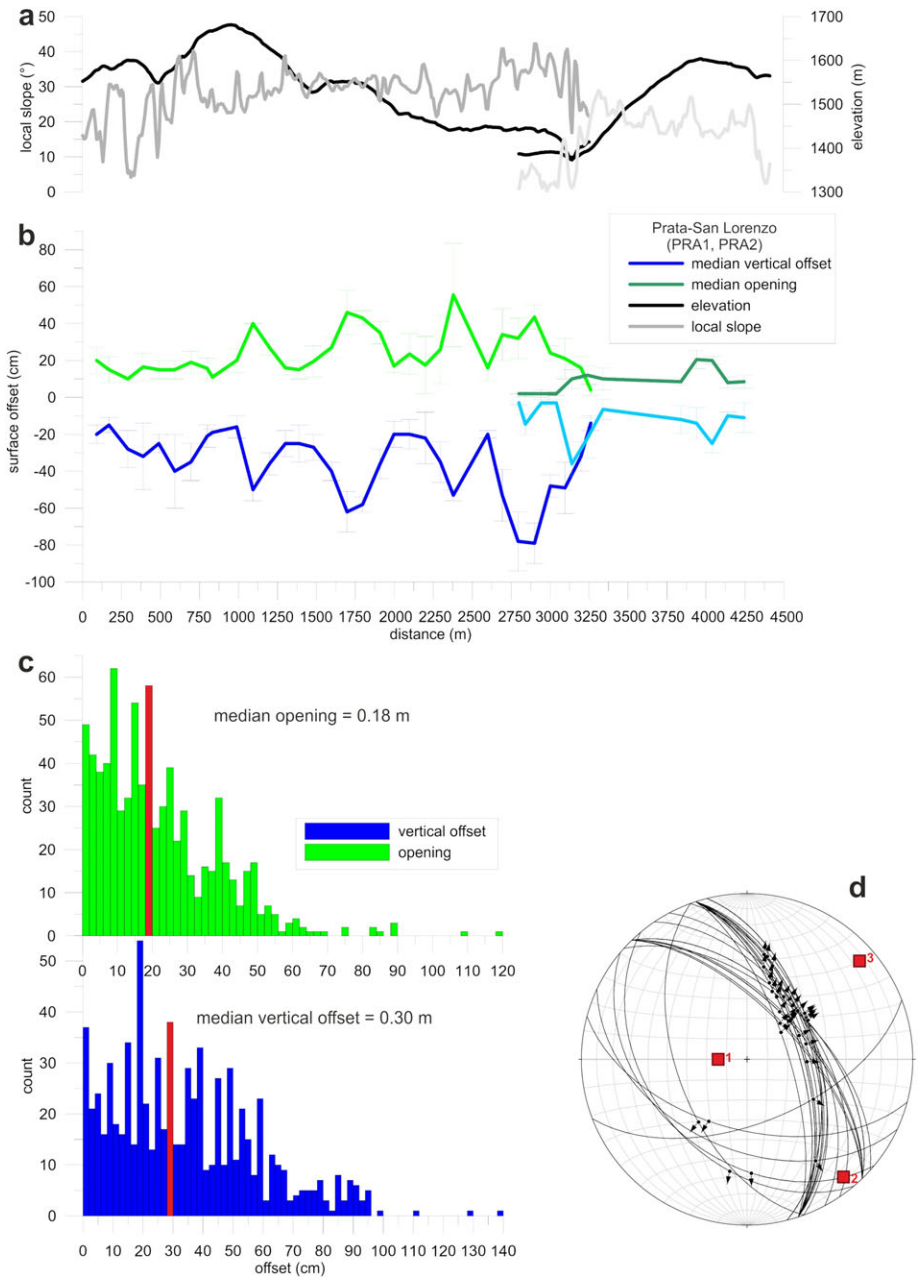

Figure 5. Prata subsegment (splays PRA1 and PRA2). a) Absolute elevation and local slope along the trace of the coseismic rupture (note the overlap of the two sections). b) Vo-x and O-x curves (error bars = ±1 MAD) of the different sections. c) Frequency histogram of coseismic ruptures (green: Opening; blue: Vertical offset). Red bars indicate median values. d) Stereoplot of coseismic slip vectors on bedrock fault planes ($N = 36$). The three kinematic axes are indicated with numbered red squares. See details in the text.

The SW dipping normal fault of Mount Vettoretto represents the southernmost splay of the Vettore subsegment (VET5 in Figure 3d). Here the coseismic surface ruptures (consisting of >80 small strands) are ~2,900-m long, with maximum vertical offset of 0.81 m (details are in Figure S5 of the supporting information). A ~ 300-m long underlap zone separates this splay from the ruptures close to Arquata del Tronto (Figure 3d; fault splay VET7), which represent the southern tip of the Norcia earthquake surface rupture.

Surface faulting within the Pian Grande di Castelluccio basin affects the topmost alluvial fan and lacustrine infill deposits (splay VET1 in Figure 3d), at an average elevation of 1,300 m a.s.l. Such rupture is of utmost

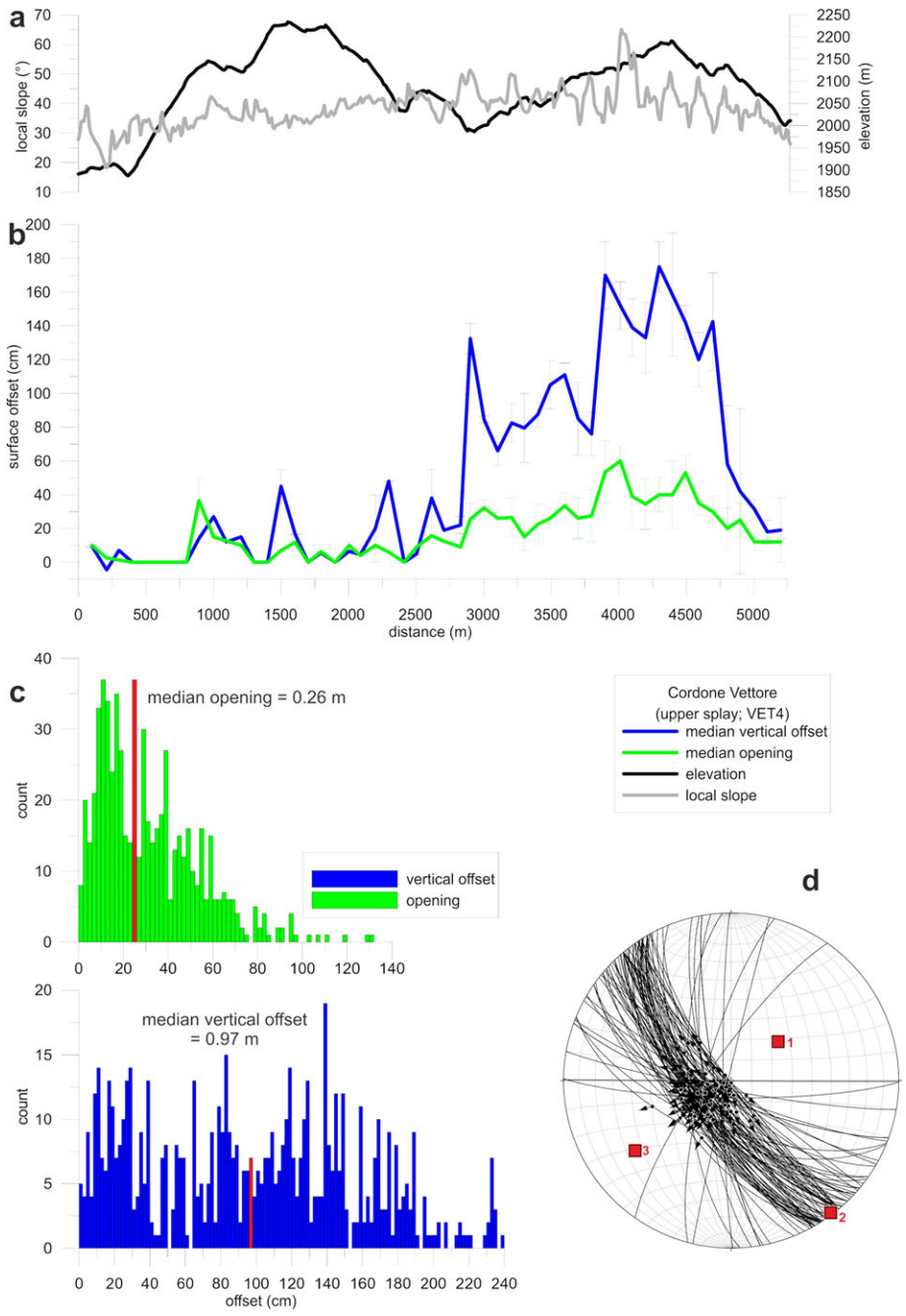

Figure 6. Vettore subsegment: Cordone del Vettore splay (VET4). (a) Absolute elevation and local slope along the trace of the coseismic rupture. (b) *Vo-x* and *O-x* curves (error bars = ±1 MAD). (c) Frequency histogram of coseismic ruptures (green: opening; blue: vertical offset). Red bars indicate median values. (d) Stereoplot of coseismic slip vectors on bedrock fault planes (N = 105). The three kinematic axes are indicated with numbered red squares. See details in the text. MAD = median absolute deviation.

importance, since it occurs exactly where Galadini and Galli (2003) dug three paleoseismic trenches that revealed surface-rupturing Holocene paleo-earthquakes. The VET1 rupture comprises two principal right-stepping strands, with an overall length of ~1,800 m (Figure 3d), a ~450-m long underlap in the northern sector, prevalent western side down (a ~40-m-long NE dipping strand occurs in the central part), and is located at the base of a 1.4- to 2.8-m high cumulative fault scarp. In the basin (Figure S6 in the supporting information), the median coseismic vertical offset is 0.05 ± 0.02 m. The *Vo-x* curve shows three localized

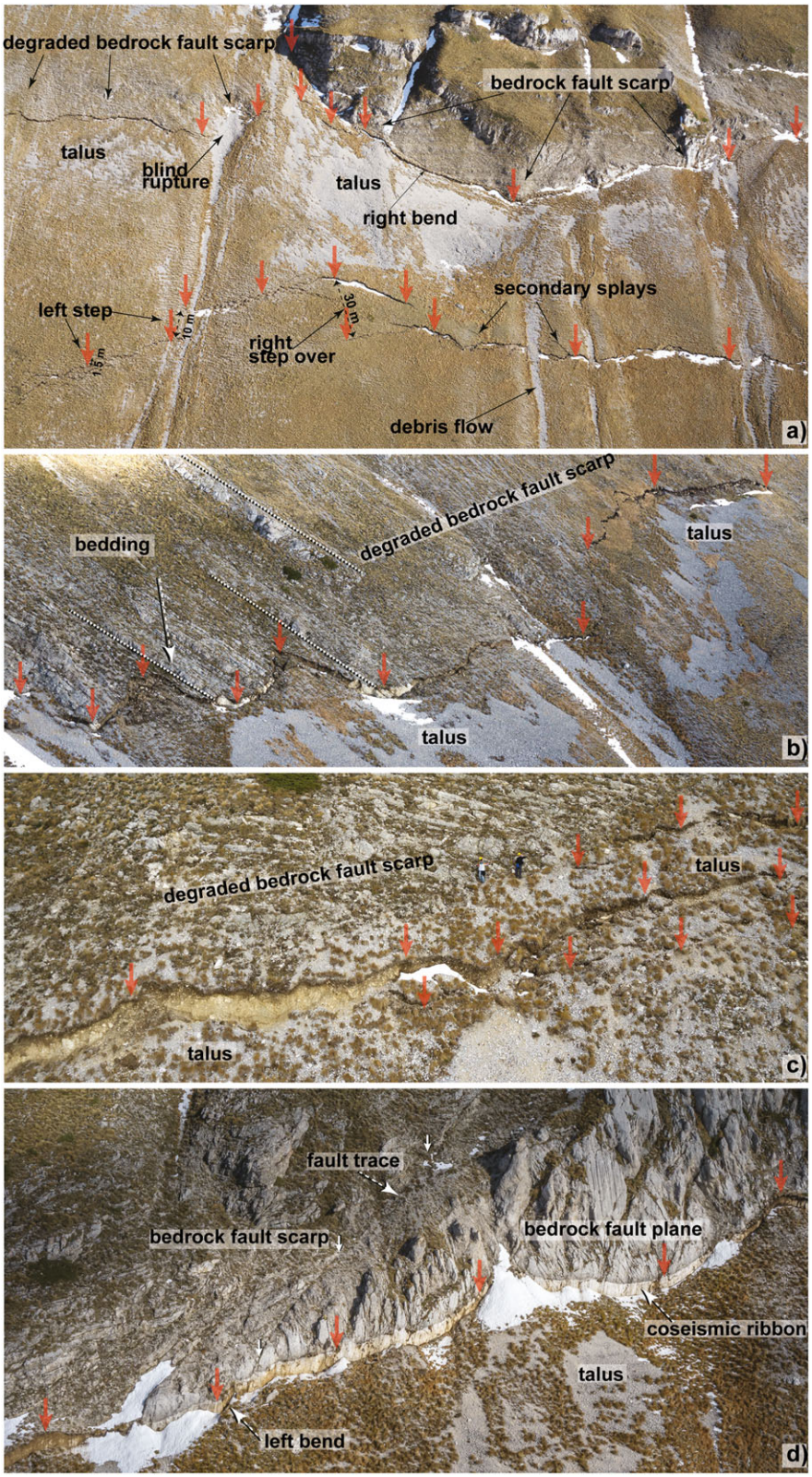

Figure 7. Selection of oblique-view photographs from helicopter, showing some details of the complex geometry and structural pattern of coseismic surface ruptures (Cordone del Vettore fault, VET4 in Figure 3). The small blind strand in Figure 7a has a very shallow upper termination that did not affect the thick debris cover. Note the two persons for scale in Figure 7c. Figure 7d shows one of the zones with the largest coseismic surface slip (> 2 m). See details in the text.

Tectonics

10.1029/2018TC005175

Table 1
Summary of Coseismic Surface Slip Components Retrieved on Each of the Main Fault Splays That Ruptured During the 30 October 2016 Norcia Earthquake

Subsegment name	Rupture splay name (informal)	Splay code	Compound splay length (m)	Median vertical offset ± MAD (m)	Average vertical offset ± 1σ (m)	Maximum vertical offset (m)	Median opening ± MAD (m)	Average opening ± 1σ (m)	Maximum opening (m)	Kurt vertical offset	Skew vertical offset	Kurt opening	Skewness opening	Resolved median slip (m)
Cupi-Banditella	Cupi-Banditella	CUP1-BAN1-BAN2	7000	0.15 ± 0.05	0.14 ± 0.09	0.40	0.08 ± 0.03	0.11 ± 0.08	0.32	0.05	0.07	2.00	1.41	0.17
Bove	Cornaccione	BOV1-BOV2	2360	0.15 ± 0.10	0.16 ± 0.15	0.70	0.10 ± 0.05	0.10 ± 0.10	0.49	0.31	0.22	5.46	2.14	0.18
Bove	Bove	BOV3	5970	0.25 ± 0.10	0.30 ± 0.19	1.10	0.13 ± 0.07	0.16 ± 0.14	1.16	2.07	1.25	15.24	3.01	0.28
Porche-Argentella	Porche-Argentella	POR2	6010	0.20 ± 0.14	0.25 ± 0.22	1.00	0.13 ± 0.07	0.17 ± 0.13	1.05	−0.13	0.88	4.34	1.65	0.24
Porche-Argentella	Palazzo Borghese	POR1	1950	0.08 ± 0.06	0.07 ± 0.08	0.23	0.05 ± 0.02	0.05 ± 0.03	0.11	−0.15	0.61	−0.93	0.28	0.09
Prata	Prata-Abuzzago	PRA1	3260	0.37 ± 0.17	0.39 ± 0.25	1.40	0.23 ± 0.11	0.26 ± 0.17	1.20	2.76	0.79	18.8	1.21	0.44
Prata	San Lorenzo splay	PRA2	1610	0.11 ± 0.09	0.15 ± 0.13	0.51	0.07 ± 0.05	0.09 ± 0.08	0.33	−0.28	0.88	0.22	0.92	0.13
Vettore	Cordone Vettore upper strand	VET4	5200	0.97 ± 0.49	0.96 ± 0.62	2.40	0.26 ± 0.14	0.32 ± 0.23	1.82	−0.74	0.09	3.77	1.43	1.00
Vettore	Cordone Vettore lower strand	VET4	1180	0.17 ± 0.09	0.25 ± 0.22	0.94	0.12 ± 0.06	0.17 ± 0.14	0.68	1.19	1.45	2.51	1.64	0.21
Vettore	Diagonal splay	VET2	2890	0.39 ± 0.24	0.46 ± 0.33	1.42	0.20 ± 0.12	0.26 ± 0.21	1.21	−0.39	0.68	1.29	1.23	0.44
Vettore	Vettoretto	VET5	2920	0.21 ± 0.13	0.25 ± 0.19	0.81	0.13 ± 0.07	0.15 ± 0.12	1.00	−0.13	0.70	8.06	1.92	0.25
Vettore	Antithetic splay	VET3	1010	0.17 ± 0.06	0.19 ± 0.11	0.50	0.06 ± 0.04	0.08 ± 0.07	0.30	1.56	1.01	2.02	1.48	0.18
Vettore	Colli Alti strand	VET2	1750	0.18 ± 0.14	0.26 ± 0.23	1.00	0.11 ± 0.07	0.16 ± 0.14	0.83	0.19	1.74	2.57	1.55	0.21
Vettore	Colli Bassi strand	VET2	720	0.08 ± 0.04	0.08 ± 0.06	0.22	0.05 ± 0.02	0.06 ± 0.03	0.14	−0.37	0.43	0.25	0.85	0.09
Vettore	Castelluccio strand	VET1	1380	0.05 ± 0.02	0.06 ± 0.04	0.14	0.01 ± 0.01	0.015 ± 0.015	0.07	0.30	0.21	−0.15	0.73	0.05
Vettore	Forca di Presta	VET6	1890	0.03 ± 0.03	0.07 ± 0.10	0.31	0.06 ± 0.04	0.07 ± 0.07	0.29	0.43	0.47	0.72	0.99	0.07
Vettore	Arquata	VET7	640	0.09 ± 0.01	0.08 ± 0.06	0.16	0.06 ± 0.02	0.07 ± 0.04	0.12	N.A.	N.A.	N.A.	N.A.	0.11

Note. We also include fault splays of the Viss.o earthquake CUP1, BAN1, and BAN2, which we treat together as a unique subsegment (Cupi-Banditella). See details in the text and Figure 3 for the location of the main rupture subsegments

Table 2
Summary of the Retrieved Kinematic Axes Retrieved From Inversion of Coseismic Slip Vectors for the Main Rupture Splays

Subsegment	Splays	*N* data	S1 (trend/plunge)	S2 (trend/plunge)	S3 (trend/plunge)
Cupi-Banditella	CUP1-BAN1-BAN2	9	43°/60°	139°/4°	231°/30°
Bove	BOV3	19	51°/81°	150°/1°	240°/9°
Porche-Argentella	POR1-POR2	48	50°/78°	146°/1°	236°/12°
Prata	PRA1-PRA2	36	271°/76°	141°/9°	49°/11°
Vettore	VET4	105	50°/60°	143°/2°	234°/30°
Vettore	VET5	24	34°/79°	138°/3°	229°/10°

Note. S1 is the shortening axis, S2 is the intermediate axis, and S3 is the extension axis. See details in the text.

maxima, occurring at 800, 1,400, and 1,800-m along-strike distance, with local maximum vertical offset values of 0.09, 0.14, and 0.08 m, respectively (details in Villani & Sapia, 2017).

Among tens of field examples, we select some representative oblique-view photographs from helicopter (Figures 7 and 8) to describe the arrangement and complexity of the coseismic surface ruptures of the Norcia earthquake.

Ruptures segmentation is visible at a wide range of scales. They are composed of several subparallel, often overlapping, strands and include underlap areas of variable size (ranging from a few meters up to >500 m in length). Tens of relay zones contribute to transfer brittle deformation between adjacent ruptures. Usually, rupture terminations are characterized by relatively narrow relays (from a few decimeters to a few tens of meters wide), or they exhibit marked bends (Figure 7a). At the outcrop scale, in several locations we observe ramps at overstepping strands, and the summed throws within the relay zones indicate a preservation of slip along adjacent strands.

From a general point of view, ruptures with southwestern downthrown side often display a right-stepping arrangement, and accordingly we observe a prevalent left-stepping relationship between overlapping ruptures with northeastern downthrown side. However, more detailed field observations reveal local exceptions, since the morphology may influence the geometric and stepping relationships between adjacent fault strands. Further geometric complexity is due to the occurrence of bends. Some ruptures clearly follow the trend of preexisting faults (Figures 7a and 7d) or are locally controlled by the structural anisotropy of the underlying bedrock (such as bedding planes in Figure 7b). In other cases, their curvilinear shape is apparent, due to the intersection of the subplanar faults with a bumpy surface topography. Figure 8a depicts a typical example, where the rupture appears curvilinear due to its intersection with the convex western slope of Mount Porche (fault splay POR1).

Normal-faulting ruptures are mode-III shear cracks; however, depending on their intersection with topography they may appear as mode-II shear cracks with structural features resembling those of strike-slip faults. In this regard, Figures 8b and 8c show details of a highly fragmented and curvilinear rupture with SW side down (fault splay VET2 in Figure 3d). There the principal displacement zone results from the envelope of differently orientated strands, giving rise to geometrical complexity and segmentation with a pronounced right bend in the middle part. The collected coseismic kinematic indicators at this site (small blue arrows in Figures 8b and 8c) show a constant ~N250° hanging wall slip direction, independent of the strike changes of the rupture. Therefore, a pronounced left-oblique component develops in the right beds (thin double arrows in Figures 8b and 8c), promoting *P* shear extensional splays organized in a left-stepping relationship (Figure 8c).

4.2. Directional and Length Properties of Coseismic Ruptures

We show the rose diagrams of the azimuth of all the coseismic ruptures measured in the field in two main separate classes: (1) ruptures on bedrock (coseismic ribbons; Figure 9a) and (2) ruptures in loose sediments (Figure 9b). The modal strikes fall, for both classes, in the range N135–160° (SW dipping system). However, they also exhibit an important subordinate modal class in the range N320–345° (NE dipping system). Ruptures on bedrock have less azimuthal dispersion with respect to those affecting loose soils. Local variations in trend strictly follow the structural framework of the mapped VBFS splays (rose diagram in Figure 9c).

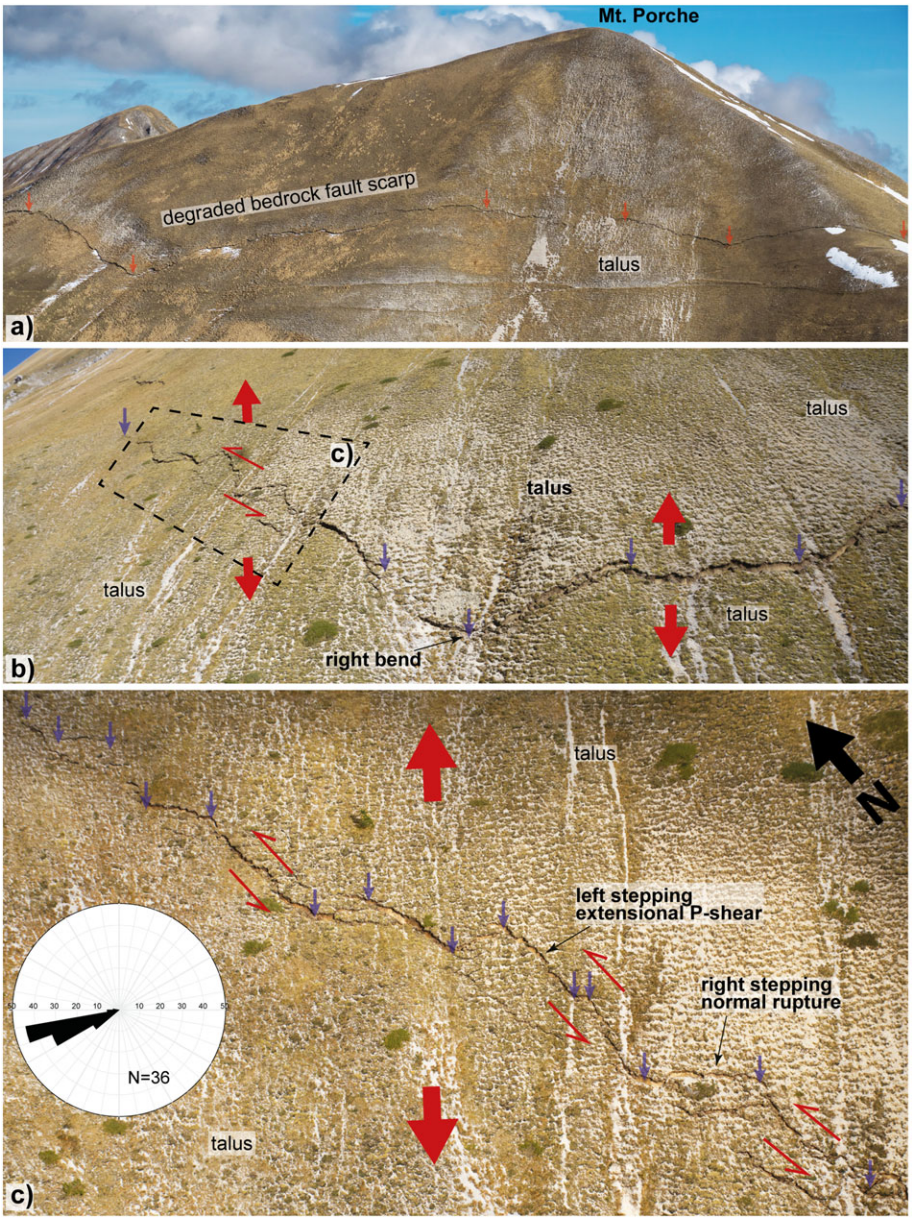

Figure 8. Selection of oblique-view photographs from helicopter, showing some details of the complex pattern of surface ruptures. (a) Rupture along the western slope of Mount Porche (indicated by thin red arrows). (b) Complex rupture on the western flank of Mount Vettore-Redentore (*diagonal*, fault splay VET2 in Figure 2): The small blue arrows indicate coseismic hanging wall slip direction, the big red arrows the general extension direction, and the thin double arrows the local oblique-slip motion. (c) Detail of the complex rupture shown in Figure 8b (note the rotated north arrow), with inset rose diagram of local slip vector directions (shown in percent frequency).

According to the map by Civico et al. (2018), the overall surface rupture (excluding ~2.7 km of ruptures that the authors indicate as due to shallow landsliding) is composed of >800 individual strands. They range in length between ~1 and 1195 m (with an average value of ~60 m), for a summed length of ~44.1–46.8 km (Figure 9d).

The cumulative frequency-length distribution of the surface ruptures (Figures 9e and 9f) indicates the occurrence of a power law scaling of the form

$$N(L) \propto L^{-a}$$

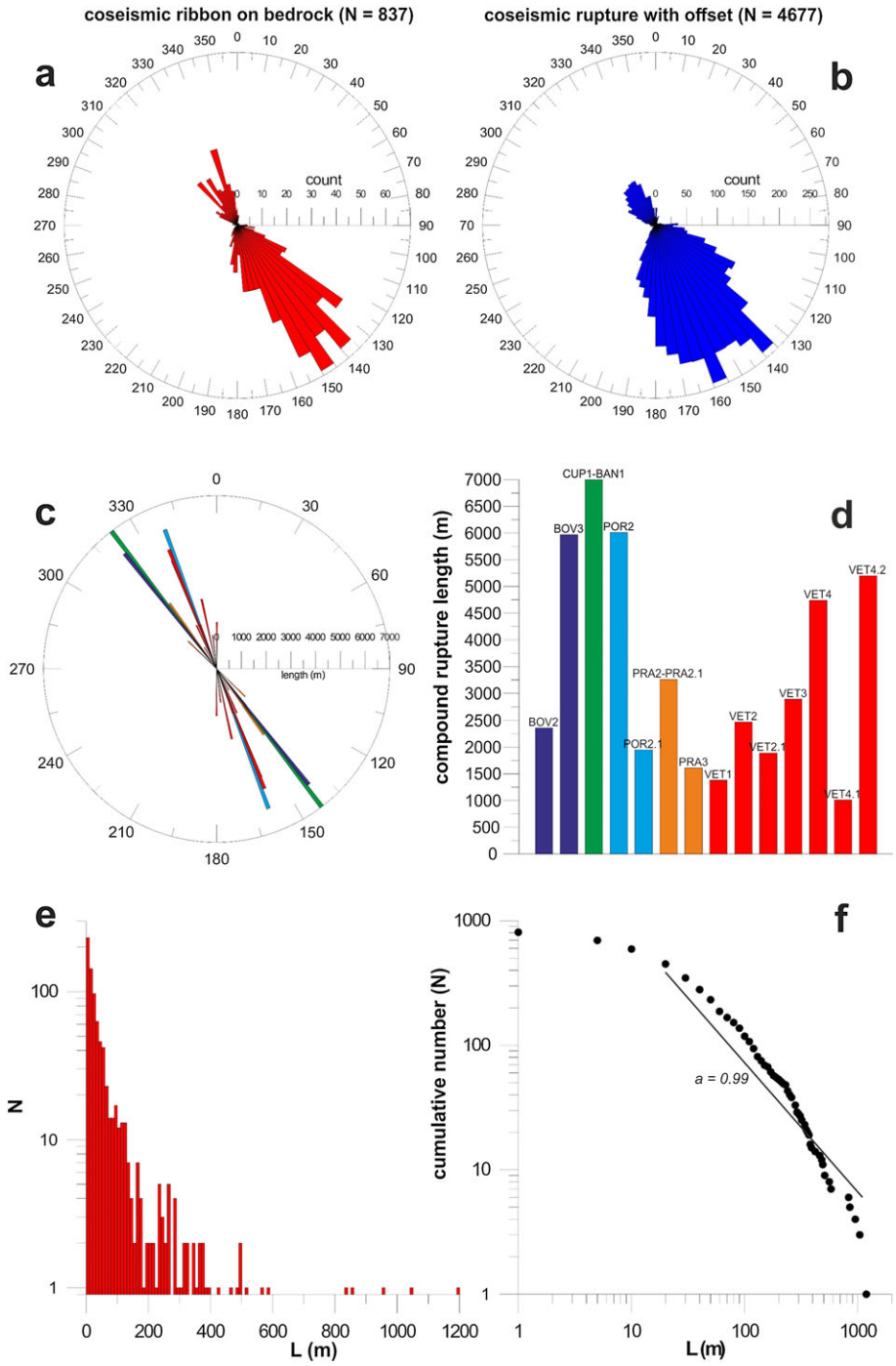

Figure 9. Rose diagrams showing the azimuthal distribution of ruptures in (a) bedrock (red) and (b) unconsolidated deposits (blue; modified after Villani et al., 2018). (c) Rose diagram of the azimuthal distribution of the previously mapped surface ruptures. (d) Bar plot of the compound length of the main splays composing the coseismic ruptures. (e) Frequency histogram of the length of the mapped individual rupture strands and (f) cumulative frequency plot of their length. See details in the text.

(where N is the number of ruptures with length equal or greater than L, and a is the scaling exponent), which we observe only within the limited spatial bandwidth of ~20–1200 m.

Eight main splays are >500 m long (along Mount Argentella, Mount Bove, Mount Prata, and Mount Vettore), and only two of them are >1,000 m in length (along Mount Vettore and Mount Bove), whereas ~95% of the

rupture strands are <250-m long. In our case, the scaling exponent a ~1 (consistent with results from some normal fault populations: Knott et al., 1996; Nicol, Walsh et al., 1996; Scholz et al., 1993 for a review) suggests that the overall strain is accommodated by a few large fault strands. Similar frequency-size distributions are observed in many studies of fault surface topography and fault length patterns (Candela et al., 2011; Sanderson & Nixon, 2015; Scholz, 2002), confirming the general power law scaling of the geometric and textural properties of fault zones (Ben-Zion & Sammis, 2003; Cowie et al., 1995).

4.3. Spatial Distribution and Kinematics of Coseismic Surface Slip

We use ~5,200 measurements of vertical offset and opening (Figures 10a and 10b) to derive the *Vo-x* and *O-x* curves of the coseismic ruptures. The frequency histograms (Figures 10c and 10d) point out the occurrence of complex distributions, as a consequence of the fact that slip on natural faults is spatially heterogeneous at a wide range of scales (Scholz, 2002).

Within a limited bandwidth (about 2 orders of magnitude), these data follow an exponential distribution (Figures 10e and 10f) of the general form:

$$N(S) = N_0 \exp(-\beta S)$$

The equation indicates that the cumulative number of data N with slip $> S$ decays from the total N_0 cumulative value according to the scaling exponent β. The average of the exponential distribution of a random variable is equal to $1/\beta$: in our case, the result is ~0.39 and ~0.17 m for vertical offset and opening, respectively, very close to the arithmetic means (Figures 10c to 10f). The two distributions are truncated for values of vertical offset and opening >2.30 and > 1.30 m, respectively, evidencing the approaching to a physical upper limit for those quantities in this tectonic context.

Kinematic plots for specific rupture splays are in Figures 4–6. The average local direction of extension along the five subsegments (Table 2) is also shown in Figure 11.

By using 241 coseismic kinematic data from bedrock fault planes of the five subsegments, we obtain an extension axis trending N233° (Figure 11, inset). The results are consistent with seismological data (section 2) and show that, notwithstanding some changes in strike of the VBFS, the retrieved local direction of extension throughout the investigated splays is nearly constant.

However, a marked short-wavelength variability of kinematics is found at local scale. An example is in Figure 12a that shows slip rake and net slip values from a ~2.2-km-long portion of fault splay VET4. The mean slip rake is −92°, a value very close to pure dip slip, and the retrieved local extensional axis trends N234° (Table 2). However, slip rake is quite variable, with deviations from the mean value that are locally >25°. The fault slip rake and slip vector trend change in order to preserve the local N234° trending local extension: therefore, the fault kinematics changes from left oblique to right oblique accordingly (Figure 12b).

4.4. Aggregate Slip of the Coseismic Surface Ruptures

Assuming that vertical offset and opening of surface ruptures are reliable proxies for fault net throw and heave, respectively, we sum the *Vo-x* and *O-x* curves of the 17 main rupture splays (Table 1) to obtain two separate cumulative *T-x* (throw) and *H-x* (heave) curves (Figure 13), projected onto a common baseline parallel to the VBFS (A-A′, in Figure 1). The projected rupture length is ~27.9 km, which is obviously a minimum estimate of the true overall surface rupture length, due to its geometric complexity.

We combine throw and heave values to obtain the aggregate coseismic surface slip curve (*S-x*) projected onto baseline A–A′, which takes into account the contribution of the entire surface ruptures produced by the three major shocks of the seismic sequence (Figure 14a). Since the kinematic data indicate a dominant dip-slip motion on the investigated faults (section 4.3), we can assume that the retrieved dip slip is nearly equal to the net surface slip.

In the *S-x* curve, we distinguish the contribution of the three events, although this is not an easy task and some uncertainties exist. For the Amatrice earthquake, we take advantage of the detailed data by Pucci et al. (2017). As discussed earlier our field surveys for the Visso earthquake are incomplete; thus, we infer it likely involved only the northernmost part of the VBFS (faults splays CUP1, BAN1, and BAN2 in Figure 3a).

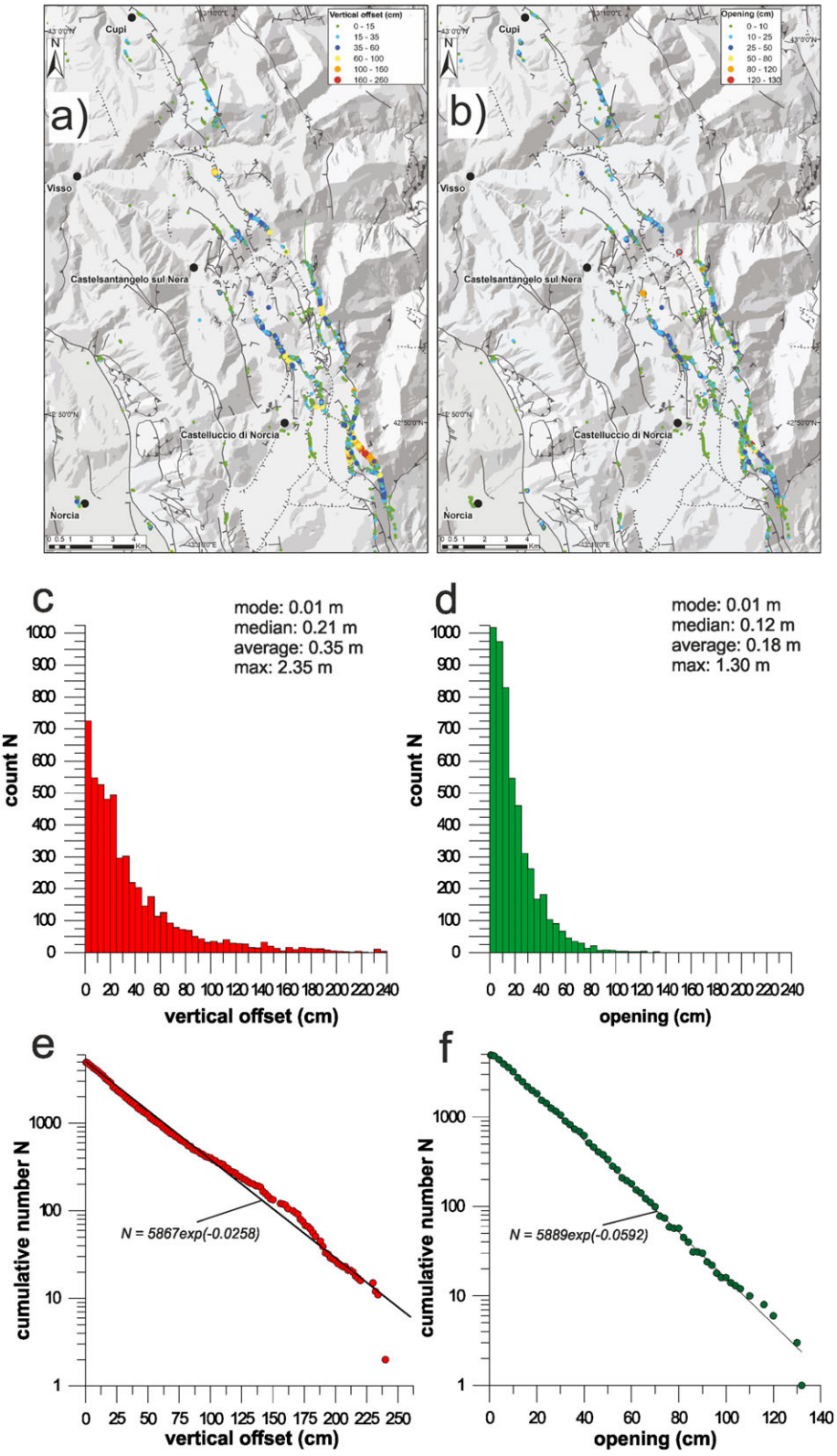

Figure 10. Coseismic vertical offset and opening following the Norcia earthquake. Map view of the collected data points ([a] vertical offset; [b] opening). Frequency histogram plots (bin size 5 cm) of vertical offset (c) and opening (d). Cumulative frequency plots (with exponential best fit curve) of vertical offset (e) and opening (f). See details in the text.

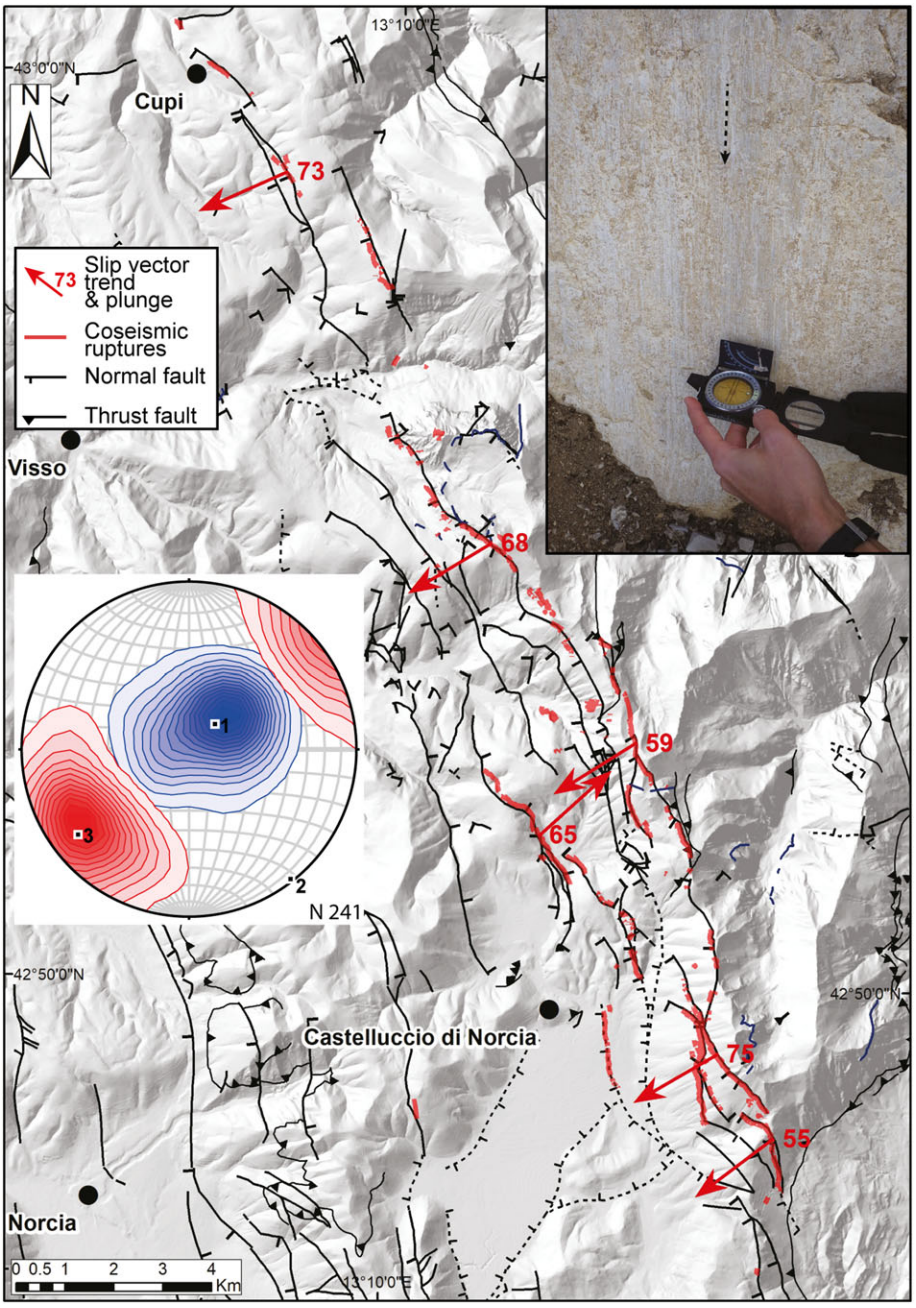

Figure 11. Map view plot of average slip vectors calculated for the main rupture subsegments from the individual slip data (we show separate average slip vectors for splays VET4 and VET5 of the Vettore subsegment). The inset picture (upper right) shows an example of kinematic indicators: Mud smears and fresh striations on the fault plane (splay VET4, date: 22 November 2016) that record coseismic motion with almost pure dip slip (black dashed arrow). The inset stereoplot shows the results of linked Bingham analysis of 241 slip vectors (blue for compression and red for extension axes; contour interval = 20) from which we obtain S1 45°/72°, S2 142°/0°, and S3 233°/18°.

The incomplete survey of splay BOV2 also affects the correct estimation of total slip of the Norcia earthquake in this sector.

The *S-x* curve of the Norcia earthquake shows a striking asymmetry, with maxima concentrated in a relatively short section located in the southernmost part of the activated VBFS (fault splays VET2, VET4, and VET5 in Figure 3d), at x = 23.5–26 km along the baseline A–A′. The high slip peaks (>1.5 m) along the Cordone del Vettore fault splay occur on a relatively small (~2.5-km long) portion of a ~22-km long surface rupture. The

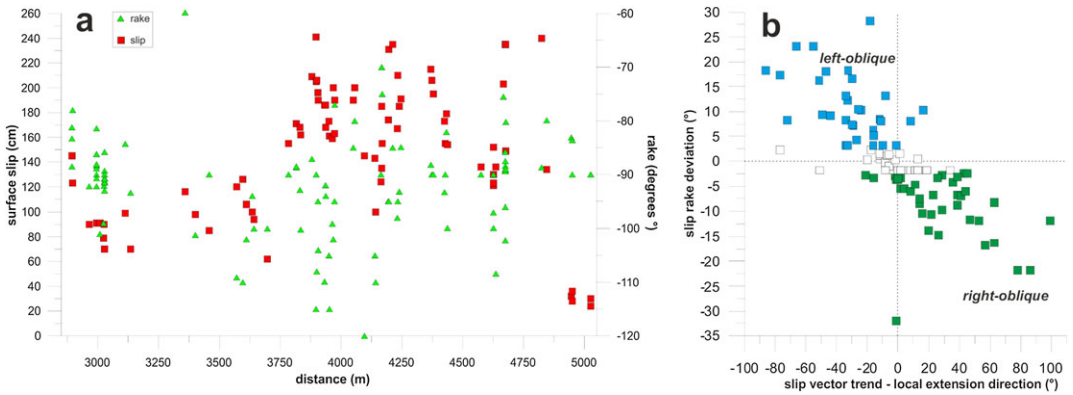

Figure 12. (a) Net coseismic surface slip (red squares) and coseismic slip rake (green triangles) versus along-strike distance of the Cordone del Vettore fault (splay VET4). (b) Angular deviation of rake from average rake value versus angular deviation of slip vector trend from average local extension direction (N234°): Blue squares indicate dominantly left-oblique motion, green squares indicate dominantly right-oblique motion, and white squares indicate nearly pure dip slip. See details in the text.

Cordone del Vettore splay (VET4) contributes to a large proportion (~40%) of the total surface slip. The complex pattern of the surface slip is evidenced by at least three large-scale secondary slip maxima (at x = 10, 13, and 18 km, respectively). The complexity of surface slip in the central part of the rupture is partly due also to important antithetic throws along fault splays PRA1 and PRA2.

In Figure 14b, we show the width of the surface deformation zone following the Norcia earthquake measured as the maximum horizontal distance between the westernmost and easternmost rupture splays orthogonal to baseline A–A′. In general, such width increases in the central and southern part of the surface rupture, where the overall amount of slip increases significantly as well.

5. Discussion

5.1. Surface Slip of the Norcia, Visso, and Amatrice Earthquakes

Based on the results described in the previous sections, we discuss the general properties of the coseismic surface ruptures and their relations with the deep seismogenic source. Table 3 summarizes the slip characteristics of the three main earthquakes of the seismic sequence.

The coseismic ruptures of the Amatrice earthquake are due to the activation at the surface of fault splays VET4 and VET5, with an average surface slip S_{avg} ~0.13 m and a peak of 0.35 m (Pucci et al., 2017). The surface slip area (SA_{surf}) for this earthquake is ~630 m^2. The peak of the S-x curve is located along the Cordone del

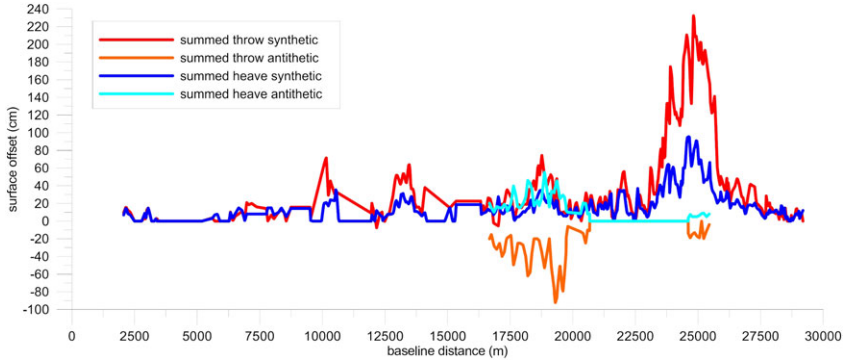

Figure 13. Summed throws (red and orange curves) and heave (dark and light blue) for the synthetic and antithetic coseismic ruptures produced by the three major earthquakes (Amatrice, Visso, and Norcia) projected onto the common baseline A–A′ shown in Figure 1. Antithetic throws are negative.

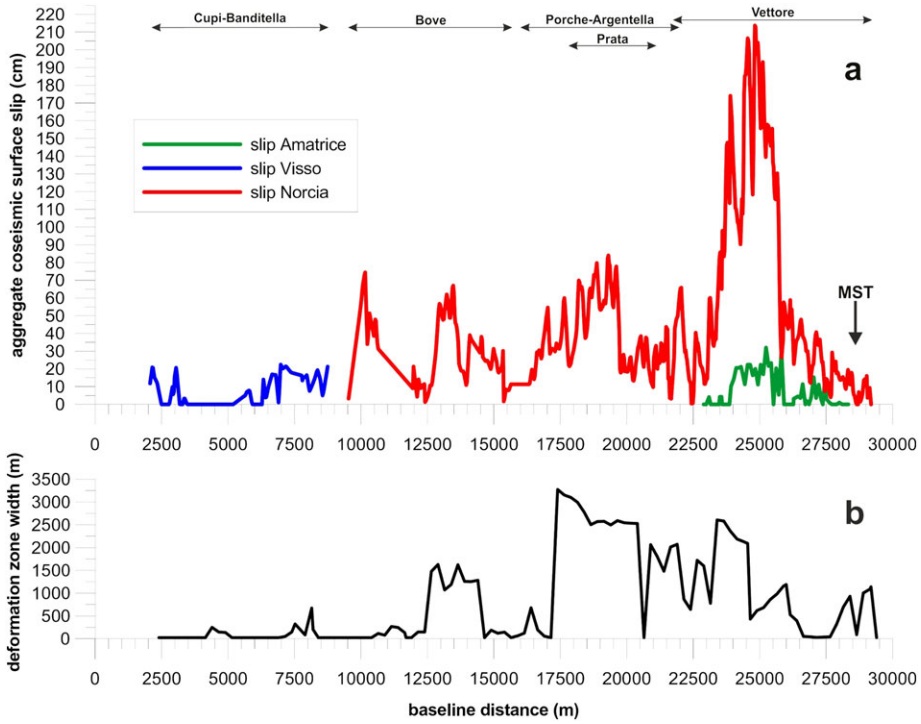

Figure 14. (a) Aggregate surface slip for the 24 August 2016 M_w 6.1 Amatrice earthquake (green curve), the 26 October 2016 M_w 5.9 Visso earthquake (blue curve), and the 30 October 2016 M_w 6.5 Norcia earthquake (red curve), projected onto the common baseline A–A′; (b) width of the surface deformation zone following the Norcia earthquake measured orthogonally to baseline A–A′. See details in the text. MST = Sibillini Mountains thrust.

Vettore fault (splay VET4). A secondary maximum is observed along the Vettoretto splay (VET5), and no surface slip occurred beyond its southern splay.

The average surface slip due to the Visso earthquake is S_{avg} ~0.11 m with a peak of 0.40 m, and the resulting surface slip area is SA_{surf} ~750 m^2. The shape of the *S-x* curve and the average slip value are likely affected by incomplete field sampling due to the occurrence of the 30 October event that drove attention and possibly overprinted those ruptures. Therefore, in this case S_{avg} represents a minimum estimate.

The Norcia earthquake involved almost all of the VBFS splays previously described, except CUP1, BAN1, and possibly BAN2. The resulting average surface slip is S_{avg} ~0.44 m with a peak S_{max} of ~2.10 m, and the resulting surface slip area is SA_{surf} ~8,470 m^2. Such surface slip peak is a rounded estimate we derived by subtracting the surface slip maximum of the Amatrice earthquake from the maximum slip measured along the Cordone del Vettore fault (section 4.1). In fact, both quakes produced the largest surface slip on the same splay VET4, and the overprinting and magnification of the Amatrice earthquake ruptures by the subsequent Norcia earthquake has been widely documented (EMERGEO Working Group, 2017; Pizzi et al., 2017; Villani et al., 2018; Walters et al., 2018). From those values, it follows that the amount of surface slip produced by

Table 3
Summary of Average Surface Slip (S_{avg}), Median Surface Slip (S_{med}), Maximum Slip (S_{max}), Surface Slip Area (SA_{surf}), and Surface Rupture Length (L_s) for the Three Mainshocks of the Seismic Sequence (This Study)

Earthquake	S_{avg} (m)	S_{med} (m)	S_{max} (m)	SA_{surf} (m^2)	L_s (m)	M_0 (N × m)
Amatrice (24 August 2016)	0.13	0.11	0.35	630	6250	1.60×10^{18}
Visso (26 October 2016)	0.11	0.12	0.40	750	7000	1.13×10^{18}
Norcia (30 October 2016)	0.44	0.30	2.10	8470	21900	8.8×10^{18}

Note. The scalar seismic moment M_0 for the Amatrice earthquake is from Tinti et al. (2016), for the Visso earthquake is from Chiaraluce et al. (2017), and for the Norcia earthquake is from Scognamiglio et al. (2018).

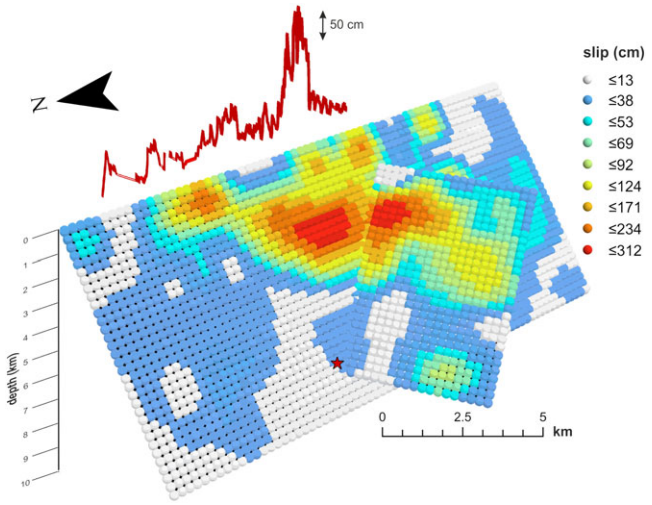

Figure 15. Perspective view (looking toward the SE: note the rotated north arrow) of the complex source model of the Norcia earthquake obtained through joint inversion of strong-motion waveforms and GPS displacements, involving the N155° trending VBFS and the N210° trending low-angle normal fault (after Scognamiglio et al., 2018). The red star indicates the hypocenter of the mainshock; the *S-x* curve is also shown on the top of the VBFS. VBFS = Mount Vettore-Mount Bove fault system; GPS = Global Positioning System.

the Norcia earthquake is 1 order of magnitude larger than the previous two quakes, and we observe a comparable scaling also for their respective scalar seismic moments (Table 3).

5.2. Relations Between Coseismic Surface and Deep Slip of the 2016 Norcia Earthquake

The coseismic surface slip of the Norcia earthquake (projected onto baseline A–A′) is compared with the overall slip at depth as inferred from the recent source model by Scognamiglio et al. (2018, Figure 15).

The multifault rupture involves the VBFS and the N210° striking low-angle normal fault in the hanging wall block (possibly due to kinematic inversion of a limited part of the southern MST), which contributes to a significant release of seismic moment. Moreover, slip on the VBFS propagates southeastward beyond the MST. Such heterogeneous deep slip distribution reflects on the surface slip; thus, the joint analysis of geological and seismological data is crucial to understand the complexity of the surface slip pattern. We observe that the surface rupture tips match the outline of the seismogenic fault area that experienced >0.6-m slip in the uppermost 2 km (some isolated patches are too deep to have caused significant effects at the surface). As regards the high peak slip along the Cordone del Vettore fault and the coseismic exhumation of this spectacular bedrock fault scarp (splay VET4), we note a broad correspondence with the two main slip patches developed onto the VBFS and the ramp portion of the MST (with peak slip of 2.8 and 3.1 m, respectively). In particular, splay VET4 exhibits a negative skewness in the frequency distribution of surface vertical offset (Table 1 and Figure 6), which stems from the great slip concentration along a very short portion of the whole rupture controlled by the main slip patch. Hence, a link between shallow slip patches and high surface slip is evident. Moreover, the whole pattern of surface faulting is consistent with the structural architecture of the normal fault array composing the VBFS. All this points out the primary tectonic origin of surface faulting. As previously discussed, results from Wilkinson et al. (2017) also clearly support primary surface faulting during the Norcia earthquake, since the near-field coseismic displacement took place at a rate comparable to the rupture propagation speed.

From Figure 14, the northernmost termination of the rupture appears very clear (at x ~9,500 m along the baseline A–A′). The trace of the Cupi-Banditella subsegment, consequently, lies to the north, outside the modeled rupture area of the Norcia earthquake source (Figure 15), and matches the extent of the main slip patch of the Visso earthquake (peak value of ~0.8 m; Chiaraluce et al., 2017). All this corroborates our hypothesis that the Cupi-Banditella subsegment slipped mostly during the Visso earthquake, and it likely did not contribute to surface slip during the Norcia event. For the same reason, we consider some discontinuous ruptures observed along fault BOV2 after the Visso earthquake as secondary features later overprinted by the primary ruptures of the Norcia earthquake.

As regards the southernmost termination of the Norcia earthquake surface rupture, we note that it completely overprints the Amatrice earthquake surface breaks and extends well beyond to the southeast (Figure 14), affecting a poorly known structure to the south of Forca di Presta and to the west of Arquata del Tronto (splay VET6 in Figure 3d). In this area there are only slight hints of surface-rupturing events predating the Norcia earthquake: in fact, the coseismic ruptures are spread and discontinuous, and they locally follow some subtle morphologies (small scarps and break in slope, aligned dolines) suggesting the presence of a normal fault dipping to the west (not reported in any geological map). Therefore, we interpret this setting as the expression of a young splay of the Vettore subsegment experiencing active growth in recent times. Scognamiglio et al. (2018) indicate the occurrence of coseismic slip during the 30 October event along the same fault area affected by the 24 August rupture, which further supports the rerupturing of the Amatrice earthquake breaks.

The southeasternmost ruptures of the Norcia earthquake cross the uppermost termination of the regional MST (splay VET7; Figures 3d and 14). This area, in the overstep zone between the VBFS and the LMFS, is

characterized by high local structural complexity, widespread debris cover, and landsliding, which hamper detailed observation of the fault pattern. The earthquake source model in Figure 15 indicates a very shallow slip patch of ~1 m, about 2 km to the southeast of the surface rupture southern tip. In this regard, Chiaraluce et al. (2017) describe the Amatrice event shallow slip patches not associated with any evidence of surface breakages along the LMFS. This suggests that the different frictional properties of the uppermost portion of the LMFS may have hindered upward rupture propagation, probably due to the shallow ~2-km thick Laga flysch, consisting of marls and sandstones (Figures 1 and 3).

5.3. Inferences on the Segmentation of the Norcia Earthquake Fault

The power law scaling of coseismic surface rupture length (Figures 10c and 10d) indicates that segmentation is an intrinsic geometric property of this fracture network, which we observe at different scales. In fact, the *S-x* curve of the Norcia earthquake points out the contribution of four main subsegments, namely Bove, Porche-Argentella, Prata, and Vettore. The evident slip minima, particularly between Vettore and Porche-Argentella subsegments, are indicative of strong interaction between adjacent faults that may have undergone linkage. The northern and southern terminations of the *S-x* curve for those subsegments are located in correspondence of structural discontinuities. In particular, the MST to the south (Figure 3d), and some WSW trending faults between the Cupi-Banditella and Bove subsegments to the north (Figures 3a and 3b) represent the most obvious outcropping transverse structures. This coincidence highlights that they play a role as long-term geological boundaries that contribute to the segmentation of the VBFS and hamper or modulate the propagation of rupture during large earthquakes.

The underlap zone between the Cupi-Banditella and Bove rupture subsegments corresponds to a long-term geologic throw deficit zone of the VBFS (Pizzi & Scisciani, 2000). The rupture history of the Visso and Norcia earthquakes (Chiaraluce et al., 2017; Scognamiglio et al., 2018) suggests that, in this particular case, fault segmentation can impede rupture propagation between adjacent faults, whatever their degree of linkage.

The southern boundary of the Norcia earthquake rupture is more complicated. Coseismic breaks cross the surface trace of the MST at depth, considered as an important segment boundary before 2016 (e.g., Pizzi & Galadini, 2009). The model by Scognamiglio et al. (2018) suggests that during the Norcia earthquake slip involved a small portion of the MST, which at the same time abuts the VBFS. The complexity of the Amatrice earthquake rupture process (Tinti et al., 2016) also raises some concern on the permanent boundary nature of the MST. We infer that the relay zone between the LMFS and the VBFS is a weak crustal volume that does not completely halt rupture propagation between those two first-order seismogenic structures. In this regard, Lavecchia et al. (2016) postulate that the VBFS and LMFS are hard linked at depth and displace the MST.

The 2016–2017 seismic sequence is a snapshot of the antagonistic long-term growth processes of two major normal fault systems, complicated by the structural heterogeneity in their relay zone, and it sheds light on the seismogenic processes acting in this part of the Apennines. The complex deep and surface slip histories of the Amatrice and Norcia earthquakes suggest strong fault interaction, and the possibility for coseismic rupture to propagate even through heterogeneous structural discontinuities.

5.4. Incremental Slip and Displacement Accumulation Along the VBFS

Due to its considerable size, the Norcia earthquake surface slip can be considered as a proxy for the typical incremental fault growth of the VBFS, useful to test the validity of earthquake recurrence (Schwartz & Coppersmith, 1984) and fault-growth models (Cowie & Shipton, 1998), and to shed light on how asperities and barriers behave in a long-term perspective (Manighetti et al., 2005).

Fault growth models from elastic-plastic fracture mechanics (Cowie & Scholz, 1992a, 1992b) and their modified versions (Cowie & Shipton, 1998), which produce bell-shaped or flat-topped slip profiles with smooth displacement gradients at fault tips, do not describe the *S-x* curve of the Norcia earthquake (Figure 14). Other fault-growth models take into account the widespread evidence of triangular slip distributions emerging from the analysis of many normal fault populations (Manighetti et al., 2001, 2009; Walsh & Watterson, 1987) and earthquake ruptures (Manighetti et al., 2005; Manzocchi et al., 2006). However, the resulting theoretical slip profiles barely fit the *S-x* curve (see details in Figure S12 of the supporting information).

The marked asymmetry of the Norcia earthquake *S-x* curve is due to a slip peak close to the southern rupture tip (at ~80% of the total fault length). The southern part shows two distinct linear portions, where the Vettore subsegment has a slip gradient >10 times higher than the Vettoretto subsegment. The northern linear taper displays a high gradient, as well. Moreover, the *S-x* curve shows evident large-scale bumps and troughs, due to heterogeneous slip concentrated on distinct subsegments. Such characteristics partly fit complex slip distributions typical of *tip-restricted* faults (Nicol et al., 2017; Nicol, Watterson et al., 1996), suggesting that the lateral tips of the VBFS may be pinned. In this regard, we note that the southern portion of the *S-x* curve may reflect the control exerted by the lateral variation of rock stiffness, due to the MST causing the juxtaposition of Meso-Cenozoic carbonates on the Miocene Laga flysch (Figures 1 and 3d). In fact, contrasting elastic moduli across fault promote high slip gradients (Bürgmann et al., 1994). As an additional cause, stress interaction with adjacent active structures (Gupta & Scholz, 2000), like the northwestern termination of the LMFS, may have also promoted the development of a high slip gradient.

The complex pattern of surface slip following the Norcia earthquake raises the question of how displacement accumulates through repeated seismic cycles over this extensional active fault system. As discussed earlier, there is a general match between large-offset coseismic surface ruptures and the highest cumulative fault scarps on the VBFS. Consistent with the main slip patches at depth, the coseismic surface slip peaks of the Amatrice and Norcia earthquakes are both located on the VET4 fault splay (Cordone del Vettore), which accounts for ~40% of the overall surface slip and, at the same time, is the largest-displacement fault within the VBFS. We observe that the additional secondary surface slip maxima are located on large-displacement faults as well (BOV, POR, and PRA splays), and the same happens with the Visso earthquake rupture (where peak slip occurs on splay BAN2). This suggests that the total amount of surface slip achieved after the three spatially and temporally clustered mainshocks of the seismic sequence mimics the general long-term displacement pattern of the VBFS. We thus infer a trend toward strain localization over a few main splays of this complex normal fault system.

In this regard, it is important to look at the recent past behavior of the VBFS. The paleoseismic data available before 2016 just concern fault splay VET1 in the Pian Grande di Castelluccio basin (Galadini & Galli, 2003). Such splay did not rupture the surface during the M_w 6.1 Amatrice earthquake, indicating that trench data in this area record only strong earthquakes and may miss some moderate ones (*M* ~6). This circumstance influences the interpretation of the paleoseismic record, because the obliteration of small surface ruptures (as in the case of the Amatrice event) by subsequent large earthquakes in very short time lapses (as in the case of the Norcia event) may complicate the reconstruction of offset and recurrence times of single paleoevents. New unpublished paleoseismic data that we acquired in 2017 along splays VET5, PRA1, and PRA2 testify that these splays repeatedly ruptured the surface with a style of deformation very similar to the 30 October 2016 event (some pictures and preliminary descriptions of the trenches are reported in the Field Trip Guide available at http://convegni.unicam.it/sites/d7.unicam.it.convegni/files/tde/GuideBookFINAL-web.pdf). In summary, paleoseismicity confirms that the VBFS growth develops during large seismic events where surface slip tends to concentrate on the same splays involved in the Norcia earthquake rupture process, including minor antithetic faults.

As regards the displacement accumulation and strain localization along the VBFS, we finally remark that the correspondence between surface slip peaks and shallow slip patches is a compelling evidence that the surface ruptures of the Norcia earthquake are primary features directly linked with the seismogenic fault at depth. In fact, their geometric and structural properties are direct expression of the coseismic rupture process, and the almost instantaneous decimetric to metric exhumation of several kilometers of fault surface (Wilkinson et al., 2017) cannot be explained by strong ground shaking nor by shallow or deep-seated gravitational phenomena. This applies also to long-term morphologies like bedrock fault scarps, which are earthquake-related morphotectonic features widespread along the VBFS and other active normal faults in the central Apennines. The Norcia earthquake demonstrates that seismic slip during large crustal earthquakes plays a major role in the genesis of bedrock fault scarps in active normal-faulting settings, and it compels to reconsider their tectonic significance in a broader perspective.

5.5. Scaling Properties of the Norcia Earthquake Surface Ruptures

Surface-rupturing earthquakes provide new tiles in the knowledge of fault growth processes and of earthquake scaling relationships (Leonard, 2010), which relate the magnitude or seismic moment with some

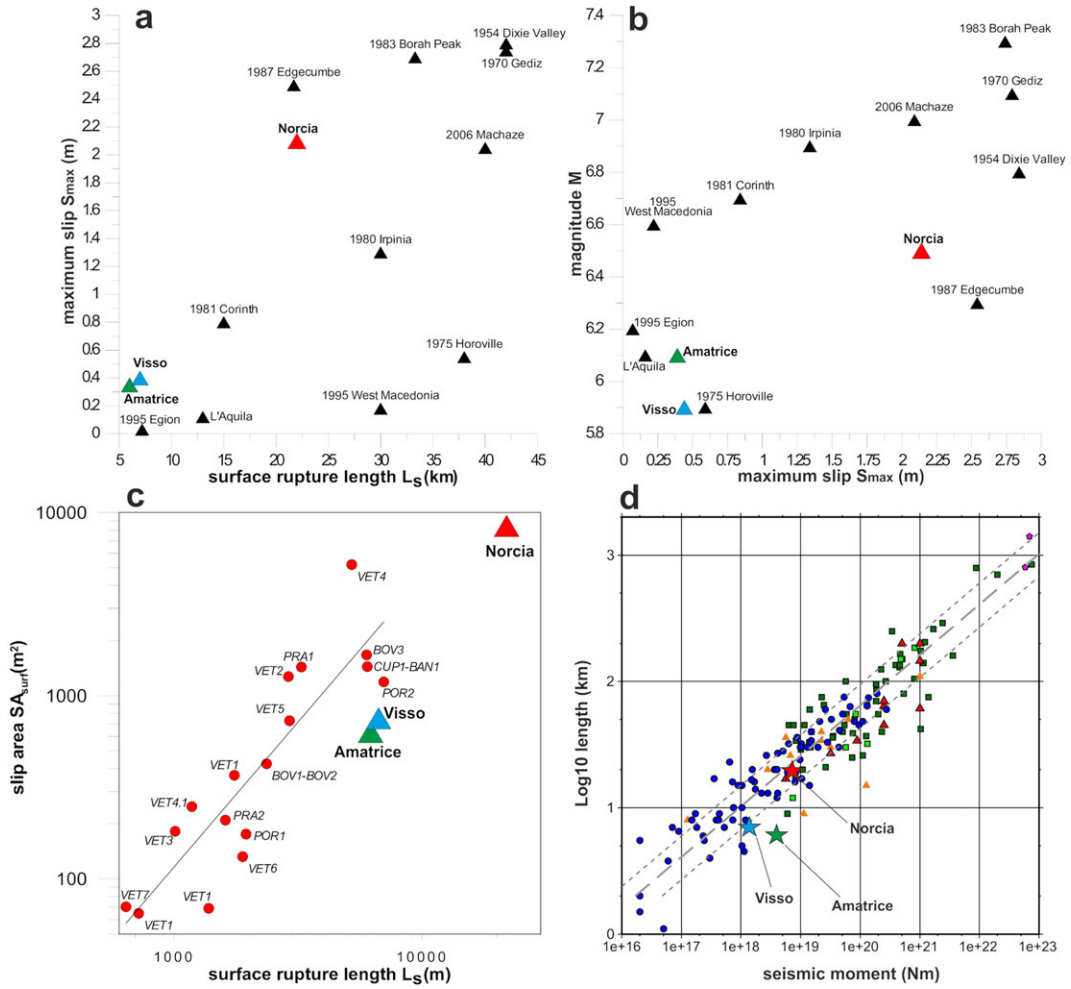

Figure 16. (a) Relation between maximum surface slip (S_{max}) and surface rupture length (L_s) for a selection of normal-faulting earthquakes (data from Boncio et al., 2012) including the 2016 Amatrice, Visso, and Norcia earthquakes (green, blue, and red triangles, respectively; data on rupture length and surface slip are from Table 3 of this work). (b) Relation between maximum surface slip (S_{max}) with earthquake magnitude for the same earthquakes shown in Figure 16a. (c) Scaling relationships for the 17 main rupture splays (red circles) analyzed in this paper and for the overall surface ruptures of the Amatrice, Visso, and Norcia earthquakes. (d) Scaling for dip-slip earthquakes (modified after Leonard, 2010), showing the consistent relation between surface rupture length versus seismic moment over a wide range of earthquake sizes (gray line: power law fit with $\beta = 2.5$; dashed lines are $\pm 1\sigma$ intervals).

first-order geometrical properties like surface rupture length and slip. Average coseismic surface slip (S_{avg}) scales with surface rupture length (L_s), and their ratio falls in the $10^{-5} < S_{avg}/L_s < 10^{-4}$ range. On the other hand, the ratio between average finite displacement (D_f) and length (L_f) of faults typically is D_f/L_f ~0.1, so that the respective constants of proportionality for S_{avg} and D_f may differ by several orders of magnitude (Kim & Sanderson, 2005; Rikitake, 1975; Sibson, 1988). As regards the Norcia earthquake, the S_{avg}/L_s ratio is ~2.0×10^{-5}, which falls within the typical range predicted by theory (Cowie & Scholz, 1992a, 1992b), and commonly observed for most surface-rupturing earthquakes.

The slip peak of the Norcia earthquake is quite high when considering its relatively short surface rupture length of 22 km and magnitude 6.5, particularly if compared with other documented normal-faulting earthquakes of similar size occurred in recent years (i.e., Table 1 in Boncio et al., 2012, and references therein). According to those data, only six other earthquakes had $S_{max} > 2$ m with L_s in the 22–42 km range, and apart from the 1987 M 6.3 Edgecumbe earthquake, all those events had magnitude >6.5 (Figures 16a and 16b). An important consequence is that normal-faulting earthquakes along the VBFS may occasionally display extreme surface-slip peak values, which apparently do not scale with the quite limited length of their

causative faults (<25 km). In addition, we compare the compound lengths of the 17 main rupture splays analyzed in section 4 with the corresponding surface slip area (SA_{surf}) in Figure 16c. The surface slip area seems to exhibit a clear scaling with rupture length according to a general power law (Scholz et al., 1993). The SA_{surf} is an integral property of the faulting process related to the total seismic moment release and is not subject to the heterogeneity of slip patches: therefore, it is statistically more robust than a single peak slip value, because it is evaluated over the whole rupture and using hundreds or thousands of measurements. We also suggest that SA_{surf} may be more useful than mean or maximum surface slip values in compiling regression analyses, although it requires very detailed field mapping and data collection (which is not always possible). This plot reveals a simple and stable geometric property of the segmented coseismic surface rupture, which as a whole represents a kinematically coherent fault population where surface rupture length scales with the surface slip area.

When compared to a large data set of dip-slip earthquakes worldwide spanning a wide range of seismic moments M_0 (Figure 16d), the surface rupture length of the Norcia earthquake pretty follows the same global power law scaling, in the general form of

$$M_0 = cL_s^{-\beta}$$

According to Leonard (2010), for dip-slip earthquakes with surface rupture $L_s > 5$ km, the scaling exponent is $\beta = 2.5$. The resulting stable regression can explain almost all the observed data (for comparison, in the same figure, we also show results for the Visso and Amatrice earthquakes).

Therefore, the scaling relations of the segmented ruptures following the Norcia earthquake reflect a constant geometric property of such coseismic fracture network, scaling with the seismic moment, and the dimensions of the seismogenic source.

6. Conclusions

We provide an analytical description of the surface ruptures of the 30 October 2016 M_w 6.5 Norcia normal-faulting earthquake, the largest seismic event striking Italy since the 1980 Irpinia M_w 6.9 earthquake.

The coseismic ruptures are nearly 22-km long and partly overprint those of the two previous earthquakes hitting Amatrice (24 August 2016, M_w 6.1) and Visso (26 October 2016, M_W 5.9), thus defining as a whole a nearly 28-km-long surface rupture along the VBFS. The total amount of surface slip for the Norcia earthquake is 1 order of magnitude larger than the Amatrice and Visso quakes.

The extreme surface slip heterogeneity reflects on a complex and skewed slip-distance curve *S-x* that shows a marked asymmetry and maxima concentrated in the southern part of the activated VBFS. Exceptionally high peak slip of ~2.1 m along the Vettore fault splay is coupled with an average surface slip of the Norcia earthquake of 0.44 m, spread over a surface slip area of about 8,500 m^2. Such surface slip peaks are strongly controlled by the heterogeneity of the rupture process at depth, which according to Scognamiglio et al. (2018) involved a multifault source with two large shallow slip patches located beneath the Vettore subsegment.

By comparing the overall surface rupture with the modeled causative mainshock source, we speculate that at least four main interacting fault subsegments contributed to surface slip during the Norcia earthquake (Bove, Porche-Argentella, Prata, and Vettore). The high gradient of the *S-x* curve at the southern termination is probably indicative of a tip-restricted normal fault system, even if rock stiffness heterogeneity and complex interaction with the adjacent Laga Mountains active fault system (LMFS) should be taken into account. Furthermore, the northern and southern terminations of the Norcia earthquake surface rupture crosscut prominent structural discontinuities, raising concern on their role as permanent segment boundaries. Seismological and geological evidence suggests that, under dynamic conditions, such barriers may be broken, probably reflecting the short-term fluctuations of an active fault growth process involving two interacting major normal fault systems (VBFS and LMFS).

The segmentation of the coseismic surface rupture is an intrinsic geometric property of this fracture network. The frequency-length distribution of the ruptures follow a power law scaling over 2 orders of magnitude. Surface offset data rather seem to follow a truncated exponential distribution. The scaling properties of

the coseismic ruptures we observe for the Norcia earthquake are in accordance with power law scaling for most of the dip-slip surface-rupturing earthquakes documented worldwide.

The close connection between coseismic surface ruptures and fault splays responsible for the generation of cumulative fault scarps suggest a progressive trend toward strain localization along a few subsegments of the complex VBFS.

As concluding remarks, the 2016 Norcia earthquake warns that some normal-faulting earthquakes in the Apennines may be occasionally associated with exceptionally high surface-slip peak values, notwithstanding the overall quite limited along-strike length of their causative faults (<25 km). Moreover, those earthquakes may rerupture the same fault portions within geologically instantaneous time windows (from a few days to weeks or months).

Acknowledgments
This work has been partly carried out in the framework of the EMERGEO Working Group activities and funded by an agreement between the Istituto Nazionale di Geofisica e Vulcanologia and the Italian Civil Protection Department (DPC-INGV 2012-2021, Allegato A). L. Gregory and C. Grützner provided insightful comments that helped us improve the quality of the manuscript. We deeply thank E. Tinti for her thoughtful comments on an early version of the draft and L. Scognamiglio for providing the fault slip model for the Norcia earthquake and useful details on the seismic sequence kinematics. We used FaultKin© software by R. Allmendiger (Allmendinger et al., 2012) to plot and analyze slip vector data. Our new unpublished structural data used in this work are available in the supporting information, while all the other data are contained in the database of coseismic effects following the 2016 Norcia earthquake: Villani, F. et al. PANGAEA https://doi.org/10.1594/PANGAEA.879469 (2017).

References

Ackermann, R. V., & Schlische, R. W. (1997). Anticlustering of small normal faults around larger faults. *Geology*, *25*(12), 1127–1134. https://doi.org/10.1130/0091-7613(1997)025<1127:AOSNFA>2.3.CO;2

Allmendinger, R. W., Cardozo, N., & Fisher, D. (2012). *Structural geology algorithms: Vectors and tensors in structural geology* (p. 302). Cambridge, UK: Cambridge University Press.

Amato, A., Azzara, R., Chiarabba, C., Cimini, G. B., Cocco, M., Diona, M., et al. (1998). The 1997 Umbria-Marche seismic sequence: A first look at the main shocks and aftershocks. *Geophysical Research Letters*, *25*(15), 2861–2864. https://doi.org/10.1029/98GL51842

Amato, A., Chiarabba, C., & Selvaggi, G. (1997). Crustal and deep seismicity in Italy (30 years after). *Annales de Geophysique*, 40–45. https://doi.org/10.4401/ag-3839

Anderson, E. M. (1951). *The dynamics of faulting and dyke formation with applications to Britain*. Edinburgh: Oliver and Boyd.

Anderson, H. J., & Jackson, J. (1987). Active tectonics of the Adria region. *Geophysical Journal of the Royal Astronomical Society*, *91*(3), 613–637. https://doi.org/10.1111/j.1365-246X.1987.tb01661.x

Barchi, M., Galadini, F., Lavecchia, G., Messina, P., Michetti, A. M., Peruzza, L., et al. (2000). Sintesi delle conoscenze sulle faglie attive in Italia Centrale: Parametrizzazione ai fini della caratterizzazione della pericolosità sismica. GNDT, Gruppo Nazionale per la Difesa dai Terremoti, Roma, spec, publ.: 62 pp.

Benedetti, L., Manighetti, I., Gaudemer, Y., Finkel, R., Malavieille, J., Pou, K., et al. (2013). Earthquake synchrony and clustering on Fucino faults (Central Italy) as revealed from in situ 36Cl exposure dating. *Journal of Geophysical Research: Solid Earth*, *118*, 4948–4974. https://doi.org/10.1002/jgrb.50299

Ben-Zion, Y., & Sammis, C. G. (2003). Characterization of fault zones. *Pure and Applied Geophysics*, *160*(3), 677–715. https://doi.org/10.1007/PL00012554

Berg, S. S., & Skar, T. (2005). Control on damage zone asymmetry of a normal fault zone: Outcrop analyses of the Moab fault, SE Utah. *Journal of Structural Geology*, *27*(10), 1803–1822. https://doi.org/10.1016/j.jsg.2005.04.012

Bernard, P., & Zollo, A. (1989). The Irpinia (Italy) 1980 earthquake: Detailed analysis of a complex normal faulting. *Journal of Geophysical Research*, *94*(B2), 1631–1647. https://doi.org/10.1029/JB094iB02p016-31

Biasi, G. P., & Wesnousky, S. (2016). Steps and gaps in ground ruptures: Empirical bounds on rupture propagation. *Bulletin of the Seismological Society of America*, *106*(3), 1110–3,1124. https://doi.org/10.1785/0120150175

Boncio, P., Galli, P., Naso, G., & Pizzi, A. (2012). Zoning surface rupture hazard along normal faults: Insight from the 2009 M_w 6.3 L'Aquila, central Italy, earthquake and other global earthquakes. *Bulletin of the Seismological Society of America*, *102*(3), 918–935. https://doi.org/10.1785/0120100301

Boncio, P., & Lavecchia, G. (2000). A structural model for active extension in central Italy. *Journal of Geodynamics*, *3-5*(29), 233–244.

Boncio, P., Lavecchia, G., & Pace, B. (2004). Defining a model of 3D seismogenic sources for seismic hazard assessment applications: The case of central Apennines (Italy). *Journal of Seismology*, *8*, 408–425.

Boncio, P., Pizzi, A., Brozzetti, F., Pomposo, G., Lavecchia, G., Di Naccio, D., & Ferrarini, F. (2010). Coseismic ground deformation of the 6 April 2009 L'Aquila earthquake (central Italy, M_w6.3). *Geophysical Research Letters*, *37*, L06308. https://doi.org/10.1029/2010GL042807

Bruhn, R. L., Gibbler, P. R., & Parry, W. T. (1987). Rupture characteristics of normal faults: An example from the Wasatch fault zone, Utah, in: Continental extensional tectonics (edited by Coward, M.P., Dewey, J.F., and Hancock, P.L.). *Special Publications Geological Society, London*, *28*(1), 337–353. https://doi.org/10.1144/GSL.SP.1987.028.01.21

Bruhn, R. L., & Schultz, R. A. (1996). Geometry and slip distribution in normal fault systems: Implications for mechanics and fault-related hazards. *Journal of Geophysical Research*, *101*(B2), 3401–3412. https://doi.org/10.1029/95JB03253

Bull, W. B. (2009). *Tectonically active landscapes*. Oxford, UK: Wiley Blackwell. https://doi.org/10.1002/9781444312003

Burbank, D. W., & Anderson, R. S. (2011). *Tectonic geomorphology*. Wiley-Blackwell. https://doi.org/10.1002/9781444345063

Bürgmann, R., Pollard, D. D., & Martel, S. J. (1994). Slip distribution on faults: Effects of stress gradients, inelastic deformation, heterogeneous rock-stiffness, and fault interaction. *Journal of Structural Geology*, *16*(12), 1675–1690. https://doi.org/10.1016/0191-8141(94)90134-1

Calamita, F., Pace, P., & Satolli, S. (2012). Coexistence of fault-propagation and fault-bend folding in curve-shaped foreland fold-and-thrust belts: Examples from the northern Apennines (Italy). *Terra Nova*, *24*(5), 396–406.

Calamita, F., & Pizzi, A. (1992). Tettonica quaternaria nella dorsale appenninica umbro-marchigiana e bacini intrappenninici associati. *Studi Geologici Camerti*, *1992*(1), 17–25.

Calamita, F., & Pizzi, A. (1994). Recent and active extensional tectonics in the southern Umbro-Marchean Apennines (central Italy). *Memoria y Sociedad Geological Italy*, *48*, 541–548.

Calamita, F., Pizzi, A., & Roscioni, M. (1992). I fasci di faglie recenti ed attive di M. Vettore – M. Bove e di M. Castello – M. Cardosa (appennino Umbro-Marchigiano). *Studi Geologici Camerti*, *1992*(1), 81–95.

Candela, T., Renard, F., Schmittbuhl, J., Bouchon, M., & Brodsky, E. E. (2011). Fault slip distribution and fault roughness. *Geophysical Journal International*, *187*(2), 959–968. https://doi.org/10.1111/j.1365-246X.2011.05189.x

Cavinato, G. P., & De Celles, P. G. (1999). Extensional basins in the tectonically bimodal central Apennines fold-thrust belt, Italy: Response to corner flow above a subducting slab in retrograde motion. *Geology*, *27*(10), 955–958. https://doi.org/10.1130/0091-7613(1999)027<0955:EBITTB>2.3.CO;2

Cello, G., Mazzoli, S., Tondi, E., & Turco, E. (1997). Active tectonics in the central Apennines and possible implications for seismic hazard analysis in peninsular Italy. *Tectonophysics*, *272*(1), 43–68. https://doi.org/10.1016/S0040-1951(96)00275-2

Centamore, E., Adamoli L., Berti D., Bigi S., Casnedi R., Cantalamessa G., et al. (1992). Carta geologica dei bacini della Laga e del Cellino e dei rilievi carbonatici circostanti (Marche meridionali, Lazio nord-orientale, Abruzzo settentrionale). Scale 1:100,000. Firenze, SELCA

Cheloni, D., De Novellis, V., Albano, M., Antonioli, A., Anzidei, M., Atzori, S., et al. (2017). Geodetic model of the 2016 central Italy earthquake sequence inferred from InSAR and GPS data. *Geophysical Research Letters*, *44*, 6778–6787. https://doi.org/10.1002/2017GL073580

Chiarabba, C., & Chiodini, G. (2013). Continental delamination and mantle dynamics drive topography, extension and fluid discharge in the Apennines. *Geology*, *41*(6), 715–718. https://doi.org/10.1130/G33992.1

Chiarabba, C., Jovane, L., & Di Stefano, R. (2005). A new view of Italian seismicity using 20 years of instrumental recordings. *Tectonophysics*, *305*, 251–268. https://doi.org/10.1016/j.tecto.2004.09.013

Chiaraluce, L. (2012). Unravelling the complexity of Apenninic extensional fault systems: A review of the 2009 L'Aquila earthquake (central Apennines, Italy). *Journal of Structural Geology*, *42*, 2–18. https://doi.org/10.1016/j.jsg.2012.06.007

Chiaraluce, L., Di Stefano, R., Tinti, E., Scognamiglio, L., Michele, M., Casarotti, E., et al. (2017). The 2016 central Italy seismic sequence: A first look at the mainshocks, aftershocks and source models. *Seismological Research Letters*, *88*(3), 757–771. https://doi.org/10.1785/0220160221

Childs, C., Holdsworth, R. E., Jackson, C. A.-L., Manzocchi, T., Walsh, J. J., & Yielding, G. (2017). Introduction to the geometry and growth of normal faults. *Geological Society of London, Special Publication*, *439*(1), 1–9. https://doi.org/10.1144/SP439.24

Choi, J.-H., Jin, K., Enkhbayar, D., Davvasambuu, B., Bayasgalan, A., & Kim, Y.-S. (2012). Rupture propagation inferred from damage patterns, slip distribution, and segmentation of the 1957 M_w 8.1 Gobi-Altay earthquake rupture along the Bogd fault, Mongolia. *Journal of Geophysical Research*, *117*, B12401. https://doi.org/10.1029/2011JB008676

Cinti, F. R., Civico, R., Blumetti, A. M., Chiarini, E., La Posta, E., Pantosti, D., et al. (2018). Evidence for surface faulting earthquakes on the Montereale fault system (Abruzzi Apennines, central Italy). *Tectonics*, *37*. https://doi.org/10.1029/2017TC004780

Cinti, F. R., Cucci, L., Marra, F., & Montone, P. (1999). The 1997 Umbria-Marche (Italy) earthquake sequence: Relationship between ground deformation and seismogenic structure. *Geophysical Research Letters*, *26*(7), 895–898. https://doi.org/10.1029/1999GL900142

Cinti, F. R., Pantosti, D., De Martini, P. M., Pucci, S., Civico, R., Pierdominici, S., et al. (2011). Evidence for surface faulting events along the Paganica fault prior to the 6 April 2009 L'Aquila earthquake (central Italy). *Journal of Geophysical Research*, *116*, B07308. https://doi.org/10.1029/2010JB007988

Civico, R., Pucci, S., Villani, F., Pizzimenti, L., De Martini, P. M., Nappi, R., & the Open EMERGEO Working Group (2018). Surface ruptures following the 30 October 2016 M_w 6.5 Norcia earthquake, central Italy. *Journal of Maps*, *14*(2), 151–160. https://doi.org/10.1080/17445647.2018.1441756

Cocco, M., Chiarabba, C., Di Bona, M., Selvaggi, G., Margheriti, L., Frepoli, A., et al. (1999). The April 1996 Irpinia seismic sequence: Evidence for fault interaction. *Journal of Seismology*, *3*(1), 105–117. https://doi.org/10.1023/A:1009771817737

Collier, R. E. L., Pantosti, D., D'Addezio, G., De Martini, P. M., Masana, E., & Sakellariou, D. (1998). Paleoseismicity of the 1981 Corinth earthquake fault: Seismic contribution to extensional strain in central Greece and implications for seismic hazard. *Journal of Geophysical Research*, *103*(B12), 30,001–30,019. https://doi.org/10.1029/98JB02643

Coltorti, M., & Farabollini, P. (1995). Quaternary evolution of the Castelluccio di Norcia Basin. *Il Quaternario*, *8*, 149–166.

Cowie, P. (1998). A healing reloading feedback control on the growth rate of seismogenic faults. *Journal of Structural Geology*, *20*(8), 1075–1087. https://doi.org/10.1016/S0191-8141(98)00034-0

Cowie, P., Phillips, R. J., Roberts, G. P., McCaffrey, K., Zijerveld, L. J. J., Gregory, L. C., et al. (2017). Orogen-scale uplift in the central Italian Apennines drives episodic behaviour of earthquake faults. *Scientific Reports*, *7*, 44858. https://doi.org/10.1038/srep44858

Cowie, P., & Scholz, C. H. (1992b). Growth of faults by accumulation of seismic slip. *Journal of Geophysical Research*, *97*(B7), 11085. https://doi.org/10.1029/92JB00586

Cowie, P. A., & Roberts, G. P. (2001). Constraining slip rates and spacings for active normal faults. *Journal of Structural Geology*, *23*(12), 1901–1915. https://doi.org/10.1016/S0191-8141(01)00036-0

Cowie, P. A., & Scholz, C. H. (1992a). Physical explanation for the displacement-length relationship of faults using a post-yield fracture mechanics model. *Journal of Structural Geology*, *14*(10), 1133–1148. https://doi.org/10.1016/0191-8141(92)90065-5

Cowie, P. A., & Shipton, Z. K. (1998). Fault tip displacement gradients and process zone dimensions. *Journal of Structural Geology*, *20*(8), 983–997. https://doi.org/10.1016/S0191-8141(98)00029-7

Cowie, P. A., Sornette, D., & Vanneste, C. (1995). Multifractal scaling properties of a growing fault population. *Geophysical Journal International*, *122*, 457–469.

Crone, A. J., Machette, M. N., Bonilla, M. G., Lienkaemper, J. J., Pierce, K. L., Scott, W. E., & Bucknam, R. C. (1987). Surface faulting accompanying the Borah Peak earthquake and segmentation of the Lost River fault, central Idaho. *Bulletin of the Seismological Society of America*, *77*(3), 739–770.

D'Agostino, N., Avallone, A., Cheloni, D., D'Anastasio, E., & Mantenuto, S. (2008). Active tectonics of the Adriatic region form GPS and earthquake slip vectors. *Journal of Geophysical Research*, *113*, B12413. https://doi.org/10.1029/2008JB005860

D'Agostino, N., Jackson, J. A., Dramis, F., & Funiciello, R. (2001). Interactions between mantle upwelling, drainage evolution and active normal faulting: An example from the central Apennines (Italy). *Geophysical Journal International*, *147*(2), 475–497. https://doi.org/10.1046/j.1365-246X.2001.00539.x

D'Agostino, N., Mantenuto, S., D'Anastasio, E., Giuliani, R., Mattone, M., Calcaterra, S., et al. (2011). Evidence for localized active extension in the central Apennines (Italy) from Global Positioning System observations. *Geology*, *39*(4), 291–294. https://doi.org/10.1130/G31796.1

D'Alessio, M. A., & Martel, S. J. (2004). Fault terminations and barriers to fault growth. *Journal of Structural Geology*, *26*(10), 1885–1896. https://doi.org/10.1016/j.jsg.2004.01.010

Dawers, N. H., & Anders, M. H. (1995). Displacement-length scaling and fault linkage. *Journal of Structural Geology*, *17*(5), 607–614. https://doi.org/10.1016/0191-8141(94)00091-D

Deschamps, A., Iannaccone, G., & Scarpa, R. (1984). The Umbrian earthquake of 19 September 1979. *Annales de Geophysique*, *2*(1), 29–36.

Devoti, R., Esposito, A., & Pietrantonio, G. (2011). Evidence of large scale deformation patterns from GPS data in the Italian subduction boundary. *Earth and Planetary Science Letters*, *311*(3–4), 230–241. https://doi.org/10.1016/j.epsl.2011.09.034

Doser, D. I. (1985). Source parameters and faulting process of the 1959 Hebgen Lake, Montana, earthquake sequence. *Journal of Geophysical Research*, *90*(B6), 4537–4555.

DuRoss, C. B., Personius, S. F., Crone, A. J., Olig, S. S., Hylland, M. D., Lund, W. R., & Schwartz, D. P. (2016). Fault segmentation: New concepts from the Wasatch fault zone, Utah, USA. *Journal of Geophysical Research: Solid Earth*, *121*, 1131–1157. https://doi.org/10.1002/2015JB012519

EMERGEO Working Group (2010). Evidence for surface rupture associated with the M_W 6.3 L'Aquila earthquake sequence of April 2009 (central Italy). *Terra Nova*, *22*(1), 43–51. https://doi.org/10.1111/j.1365-3121.2009.00915.x

EMERGEO Working Group (2016). Coseismic effects of the 2016 Amatrice seismic sequence: First geological results. *Annals of Geophysics*, *59*(5), 1–8. https://doi.org/10.4401/AG-7195

EMERGEO Working Group (2017). A new photographic dataset of the coseismic geological effects originated by the M_w 5.9 Visso and M_w 6.5 Norcia earthquakes (26th and 30th October 2016, Central Italy). *Miscellanea INGV*, *38*, 1–114. Retrieved from http://www.ingv.it/editoria/miscellanea/2017/miscellanea34/

Ferrario, M. F., & Livio, F. (2018). Characterizing the distributed faulting during the October 30, 2016, central Italy earthquake: A reference for fault displacement hazard assessment. *Tectonics*, *37*(5), 1256–1273. https://doi.org/10.1029/2017TC004935

Ferrill, D. A., & Morris, A. P. (2003). Dilational normal faults. *Journal of Structural Geology*, *25*(2), 183–196. https://doi.org/10.1016/S0191-8141(02)00029-9

Galadini, F., & Galli, P. (1999). The Holocene paleoearthquakes on the 1915 Avezzano earthquake faults (central Italy): Implications for active tectonics in the central Apennines. *Tectonophysics*, *308*(1-2), 143–170. https://doi.org/10.1016/S0040-1951(99)00091-8

Galadini, F., & Galli, P. (2000). Active tectonics in the central Apennines (Italy)—Input data for seismic hazard assessment. *Natural Hazards*, *22*(3), 225–268. https://doi.org/10.1023/A:1008149531980

Galadini, F., & Galli, P. (2003). Paleoseismology of silent faults in the central Apennines (Italy): The Mt. Vettore and Laga Mts. Faults. *Annals of Geophysics*, *46*(5), 815–836.

Galli, P., Galadini, F., & Pantosti, D. (2008). Twenty years of paleoseismology in Italy. *Earth-Science Reviews*, *88*(1), 89–117. https://doi.org/10.1016/j.earscirev.2008.01.001

Gilbert, G. K. (1890). *Lake Bonneville, U.S.G.S. Monograph 1*. Washington, DC: U.S. Government Printing Office.

Giraudi, C. (1995). Considerations on the significance of some postglacial fault scarps in the Abruzzo Apennines (Central Italy). *Quarternary International*, *25*, 33–45. https://doi.org/10.1016/1040-6182(94)00033-2

Gupta, A., & Scholz, C. H. (2000). A model of normal fault interaction based on observations and theory. *Journal of Structural Geology*, *22*(7), 865–879. https://doi.org/10.1016/S0191-8141(00)00011-0

Hamling, I. J., Hreinsdóttir, S., Clark, K., Elliott, J., Liang, C., Fielding, C., et al. (2017). Complex multifault rupture during the 2016 M_w 7.8 Kaikōura earthquake, New Zealand. *Science*, *356*, 1–10. https://doi.org/10.1126/science.aam7194

Jackson, J. A., Gagnepain, J., Houseman, G., King, G. C. P., Papadimitriou, P., Soufleris, C., & Virieux, J. (1982). Seismicity, normal faulting, and the geomorphological development of the Gulf of Corinth (Greece): The Corinth earthquakes of February and March 1981. *Earth and Planetary Science Letters*, *57*, 377–397.

Kim, Y.-S., & Sanderson, D. J. (2005). The relationships between displacement and length of faults: A review. *Earth-Science Reviews*, *68*(3-4), 317–334. https://doi.org/10.1016/j.earscirev.2004.06.003

King, G. C. P., Ouyang, Z. X., Papadimitriou, P., Deschamps, A., Gagnepain, L., Houseman, G., et al. (1985). The evolution of the Gulf of Corinth: An aftershock study of the 1981 earthquakes. *Geophysical Journal of the Royal Astronomical Society*, *77*, 915–933.

King, G. C. P., Stein, R. S., & Rundle, J. B. (1988). The growth of geological structures by repeated earthquakes 1. Conceptual framework. *Journal of Geophysical Research*, *93*(B11), 13,307–13,318. https://doi.org/10.1029/JB093iB11p13307

Knott, S. D., Beach, A., Brockbank, P. J., Brown, J. L., McCallum, J. E., & Welbon, A. I. (1996). Spatial and mechanical controls on normal fault populations. *Journal of Structural Geology*, *18*(2-3), 359–372. https://doi.org/10.1016/S0191-8141(96)80056-3

Lavecchia, G., Brozzetti, F., Barchi, M., Menichetti, M., & Keller, J. V. A. (1994). Seismotectonic zoning in east-central Italy deduced from an analysis of the Neogene to present deformations and related stress fields. *Geological Society of America Bulletin*, *106*(9), 1107–1120. https://doi.org/10.1130/0016-7606(1994)106<1107:SZIECI>2.3.CO;2

Lavecchia, G., Castaldo, R., de Nardis, R., de Novellis, V., Ferrarini, F., Pepe, S., et al. (2016). Ground deformation and source geometry of the 24 August 2016 Amatrice earthquake (central Italy) investigated through analytical and numerical modeling of DInSAR measurements and structural-geological data. *Geophysical Research Letters*, *43*, 12,389–12,398. https://doi.org/10.1002/2016GL071723

Leonard, M. (2010). Earthquake fault scaling: Self-consistent relating of rupture length, width, average displacement, and moment release. *Bulletin of the Seismological Society of America*, *100*(5A), 1971–1988. https://doi.org/10.1785/0120090189

Lin, A. (2009). Geometry and slip distribution of coseismic surface ruptures produced by the 2001 Kunlun, Northern Tipet, earthquake. In E. Fukuyama (Ed.), *Fault-zone properties and earthquake rupture dynamics*, *International Geophysics Series* (Vol. 94, pp. 15–36). Amsterdam: Academic Press, Elsevier. https://doi.org/10.1016/S0074-6142(08)00002-8

Litchfield, N. J., Villamor, P., Van Dissen, R. J., Nicol, A., Barnes, P. M., Barrell, D. J. A., et al. (2018). Surface rupture of multiple crustal faults in the 2016 M_w 7.8 Kaikōura, New Zealand, earthquake. *Bulletin of the Seismological Society of America*, *108*(3B), 1496–1520. https://doi.org/10.1785/0120170300

Livio, F. A., Michetti, A. M., Vittori, E., Gregory, L., Wedmore, L., Piccardi, L., et al. (2016). Surface faulting during the August 24, 2016, central Italy earthquake (M_w 6.0): Preliminary results. *Annals of Geophysics*, 1–8. https://doi.org/10.4401/ag-7197

Machette, M. N., Personius, S. F., Nelson, A. R., Schwartz, D. P., & Lund, W. R. (1991). The Wasatch fault zone, Utah—Segmentation and history of Holocene earthquakes. *Journal of Structural Geology*, *13*(2), 137–149. https://doi.org/10.1016/0191-8141(91)90062-N

Manighetti, I., Campillo, M., Sammis, C., Mai, P. M., & King, G. (2005). Evidence for self-similar, triangular slip distributions on earthquakes: Implications for earthquake and fault mechanics. *Journal of Geophysical Research*, *110*, B05302. https://doi.org/10.1029/2004JB003174

Manighetti, I., King, G. C. P., Gaudemer, Y., Scholz, C. H., & Doubre, C. (2001). Slip accumulation and lateral propagation of active normal faults in Afar. *Journal of Geophysical Research*, *106*(B7), 13,667–13,696. https://doi.org/10.1029/2000JB900471

Manighetti, I., Zigone, D., Campillo, M., & Cotton, F. (2009). Self-similarity of the largest-scale segmentation of the faults: Implications for earthquake behaviour. *Earth and Planetary Science Letters*, *288*(3-4), 370–381. https://doi.org/10.1016/j.epsl.2009.09.040

Manzocchi, T., Walsh, J. J., & Nicol, A. (2006). Displacement accumulation from earthquakes on isolated normal faults. *Journal of Structural Geology*, *28*(9), 1685–1693. https://doi.org/10.1016/j.jsg.2006.06.006

Marrett, R. A., & Allmendinger, R. W. (1990). Kinematic analysis of fault-slip data. *Journal of Structural Geology*, *12*, 973–986. https://doi.org/10.1016/0191-8141(90)90093-E

Meyer, V., Nicol, A., Childs, C., Walsh, J. J., & Watterson, J. (2002). Progressive localization of strain during the evolution of normal fault systems. *Journal of Structural Geology*, *24*(8), 1215–1231. https://doi.org/10.1016/S0191-8141(01)00104-3

Michetti, A. M., Brunamonte, F., Serva, L., & Vittori, E. (1996). Trench investigations of the 1915 Fucino earthquake fault scarps (Abruzzo, central Italy): Geological evidence of large historical events. *Journal of Geophysical Research*, *101*(B3), 5921–5936. https://doi.org/10.1029/95JB02852

Mildon, Z. K., Roberts, G. P., Faure Walker, J. P., & Iezzi, F. (2017). Coulomb stress transfer and fault interaction over millennia on non-planar active normal faults: The M_w 6.5-5.0 seismic sequence of 2016-2017, central Italy. *Geophysical Journal International*, *210*, 1206–1218. https://doi.org/10.1093/gji/ggx213

Mildon, Z. K., Roberts, G. P., Faure Walker, J. P., Wedmore, L. N. J., & McCaffrey, K. J. W. (2016). Active normal faulting during the 1997 seismic sequence in Colfiorito, Umbria: Did slip propagate to the surface? *Journal of Structural Geology*, *91*, 102–113. https://doi.org/10.1016/j.jsg.2016.08.011

Montone, P., Mariucci, M. T., & Pierdominici, S. (2012). The Italian present-day stress map. *Geophysical Journal International*, *189*(2), 705–716. https://doi.org/10.1111/j.1365-246X.2012.05391.x

Nicol, A., Childs, C., Walsh, J. J., Manzocchi, T., & Schöpfer, M. P. J. (2017). Interactions and growth of faults in an outcrop-scale system. In C. Childs, R. E. Holdsworth, C. A.-L. Jackson, T. Manzocchi, J. J. Walsh, & G. Yielding (Eds.), *The geometry and growth of normal faults*, *Geol. Soc. London, Spec. Publ.* (Vol. 439, pp. 23–39). https://doi.org/10.1144/SP439.9

Nicol, A., Walsh, J. J., Watterson, J., & Gillespie, P. A. (1996). Fault size distributions—Are they really power law? *Journal of Structural Geology*, *18*(2-3), 191–197. https://doi.org/10.1016/S0191-8141(96)80044-7

Nicol, A., Watterson, J., Walsh, J. J., & Childs, C. (1996). The shape, major axis orientations and displacement patterns of fault surfaces. *Journal of Structural Geology*, *18*(2–3), 235–248. https://doi.org/10.1016/S0191-8141(96)80047-2

Nixon, C. W., Bull, J. M., & Sanderson, D. J. (2014). Localized vs distributed deformation associated with the linkage history of an active normal fault, Whakatane Graben, New Zealand. *Journal of Structural Geology*, *69*, 266–280.

Oddone, E. (1915). Gli elementi fisici del grande terremoto marsicano-fucense del 13 gennaio 1915. *Bulletin de la Société Sismológico Italy*, *19*, 71–216.

Pantosti, D., De Martini, P.M., Galli, P., Galadini, F., Messina, P., Moro, M., & Sposato, A. (1999). Studi paleosismologici lungo la rottura superficiale prodotta dal terremoto del 14 Ottobre 1997 (Umbria-Marche), in Riassunti Estesi delle Comunicazioni del 18° Convegno del Gruppo Nazionale di Geofisica Della Terra Solida, 184–185, Roma 9–11 Novembre 1999.

Pantosti, D., Schwartz, D., & Valensise, G. (1993). Paleoseismology along the 1980 surface rupture of the Irpinia fault: Implications for earthquake recurrence in the southern Apennines, Italy. *Journal of Geophysical Research*, *98*(B4), 6561–6577.

Pantosti, D., & Valensise, G. (1990). Faulting mechanism and complexity of the November 23, 1980, Campania-Lucania earthquake, inferred from surface observations. *Journal of Geophysical Research*, *95*(B10), 15,319–15,341. https://doi.org/10.1029/JB095iB10p15319

Peacock, D. C. P., & Sanderson, D. J. (1991). Displacements, segment linkage and relay ramps in normal fault zones. *Journal of Structural Geology*, *13-6*, 721–733.

Pierantoni, P. P., Deiana, G., & Galdenzi, S. (2013). Geological map of the Sibillini Mountains (Umbria-Marche Apennines, Italy). *Italian Journal of Geosciences*, *132*(3), 497–520.

Pizzi, A., Calamita, F., Coltorti, M., & Pieruccini, P. (2002). Quaternary normal faults, intramontane basins and seismicity in the Umbria-Marche-Abruzzi Apennine Ridge (Italy): Contribution of neotectonic analysis to seismic hazard assessment. *Bulletin de la Société Geology Italy Special Issue*, *1*, 923–929.

Pizzi, A., Di Domenica, A., Gallovič, F., Luzi, L., & Puglia, R. (2017). Fault segmentation as constraint to the occurrence of the main shocks of the 2016 central Italy seismic sequence. *Tectonics*, *36*, 2370–2387. https://doi.org/10.1002/2017TC004652

Pizzi, A., & Galadini, F. (2009). Pre-existing cross-structures and active segmentation in the northern-central Apennines (Italy). *Tectonophysics*, *476*, 304–319. https://doi.org/10.1016/j.tecto.2009.03.018

Pizzi, A., & Scisciani, V. (2000). Methods for determining the Pleistocene–Holocene component of displacement on active faults reactivating pre-Quaternary structures: Examples from the central Apennines (Italy). *Journal of Geodynamics*, *29*, 445–457.

Pondrelli, S., Salimbeni, S., Ekström, G., Morelli, A., Gasperini, P., & Vannucci, G. (2006). The Italian CMT dataset from 1977 to the present. *Physics of the Earth and Planetary Interiors*, *159*(3–4), 286–303. https://doi.org/10.1016/j.pepi.2006.07.008

Pucci, S., De Martini, P. M., Civico, R., Villani, F., Nappi, R., Ricci, T., et al. (2017). Coseismic ruptures of the 24 August 2016, M_w 6.0 Amatrice earthquake (central Italy). *Geophysical Research Letters*, *44*, 2138–2147. https://doi.org/10.1002/2016GL071859

Rikitake, T. (1975). Statistics of ultimate strain of the Earth's crust and probability of earthquake recurrence. *Tectonophysics*, *26*(1-2), 1–21. https://doi.org/10.1016/0040-1951(75)90110-9

Roberts, G. P. (1996). Noncharacteristic normal faulting surface ruptures from the Gulf of Corinth, Greece. *Journal of Geophysical Research*, *101*(B11), 25,255–25,267. https://doi.org/10.1029/96JB02119

Roberts, G. P., Cowie, P., Papanikolou, I., & Michetti, A. M. (2004). Fault scaling relationships, deformation rates and seismic hazards: An example from the Lazio–Abruzzo Apennines, central Italy. *Journal of Structural Geology*, *26*(2), 377–398. https://doi.org/10.1016/S0191-8141(03)00104-4

Rovida, A., Locati, M., Camassi, R., Lolli, B., & Gasperini, P. (Eds.) (2016). CPTI15, the 2015 version of the parametric catalogue of Italian earthquakes. *Istituto Nazionale di Geofisica e Vulcanologia*. https://doi.org/10.6092/INGV.IT-CPTI15

Sagy, A., Brodsky, E., & Axen, G. J. (2007). Evolution of fault-surface roughness with slip. *Geology*, *35*(3), 283–286. https://doi.org/10.1130/G23235A.1

Sanderson, D. J., & Nixon, C. W. (2015). The use of topology in fracture networks characterization. *Journal of Structural Geology*, *72*, 55–66. https://doi.org/10.1016/j.jsg.2015.01.005

Scholz, C. H. (2002). *The mechanics of earthquakes and faulting* (2nd ed., p. 471). Cambridge University Press. ISBN 0521655404

Scholz, C. H., Dawers, N. H., Yu, J.-Z., Anders, M. H., & Cowie, P. (1993). Fault growth and fault scaling laws: Preliminary results. *Journal of Geophysical Research*, *98*(B12), 21,951–21,961.

Schwartz, D. P., & Coppersmith, K. J. (1984). Fault behavior and characteristic earthquakes: Examples from the Wasatch and San Andreas fault zones. *Journal of Geophysical Research*, *89*(B7), 5681–5698. https://doi.org/10.1029/JB089iB07p05681

Scognamiglio, L., Tinti, E., Casarotti, E., Pucci, S., Villani, F., Cocco, M., et al. (2018). Complex fault geometry and rupture dynamics of the M_w 6.5, 30 October 2016, central Italy earthquake. *Journal of Geophysical Research: Solid Earth*, *123*, 2943–2964. https://doi.org/10.1002/2018JB015603

Segall, P., & Pollard, D. D. (1980). Mechanics of discontinuous faults. *Journal of Geophysical Research*, *85*(B8), 4337–4350. https://doi.org/10.1029/JB085iB08p04337

Shipton, Z. K., Soden, A. M., Kirkpatrick, J. D., Bright, A. M., & Lunn, R. J. (2006). How thick is a fault? Fault displacement—Thickness scaling revisited. *Earthquakes: radiated energy and the physics of faulting*, *170*, 193–198.

Sibson, R. H. (1988). Earthquake faulting as a structural process. *Journal of Structural Geology*, *11*, 1–14.
Slemmons, D. B. (1957). Geological effects of the Dixie Valley - Fairview Peak, Nevada, earthquakes of December 16, 1954. *Bulletin of the Seismological Society of America*, *47*(4), 353–375.
Stirling, M., Goded, T., Berryman, K., & Litchfield, N. (2013). Selection of earthquake scaling relationships for seismic-hazard analysis. *Bulletin of the Seismological Society of America*, *103*(6), 2993–3011. https://doi.org/10.1785/0120130052
Tarquini, S., Vinci, S., Favalli, M., Doumaz, F., Fornaciai, A., & Nannipieri, L. (2012). Release of a 10-m- resolution DEM for the Italian territory: Comparison with global-coverage DEMs and anaglyph-mode exploration via the web. *Computers & Geosciences*, *38*(1), 168–170. https://doi.org/10.1016/j.cageo.2011.04.018
Tchalenko, J. S., & Berberian, M. (1975). Dasht-e-Bayaz fault, Iran: Earthquake and earlier related structures in bedrock. *Bulletin Geological Society of America*, *86*, 703–709.
Tinti, E., Scognamiglio, L., Michelini, A., & Cocco, M. (2016). Slip heterogeneity and directivity of the M_L 6.0, 2016, Amatrice earthquake estimated with rapid finite-fault inversion. *Geophysical Research Letters*, *43*, 10,745–10,752. https://doi.org/10.1002/2016GL071263
Vai, G. B., & Martini, I. P. (Eds.) (2001). *Anatomy of an Orogen: The Apennines and adjacent mediterranean basins*, (p. 633). Dordrecht, Netherlands: Kluwer Acad. https://doi.org/10.1007/978-94-015-9829-3
Vedder, J. G., & Wallace, R. E. (1973). Map showing recently active fault breaks along the San Andreas and related faults between Cholame Valley and Tejon Pass, California, Scale 1:24,000, Geol. Misc. Invest. Map 1–574, U.S. Geol. Surv., Reston, Virginia.
Villani, F., Civico, R., Pucci, S., Pizzimenti, L., Nappi, R., De Martini, P. M., & The Open EMERGEO Working Group (2018). A database of the coseismic effects following the 30 October 2016 Norcia earthquake in central Italy. *Scientific Data*, *5*, 180,049. https://doi.org/10.1038/sdata.2018.49
Villani, F., & Sapia, V. (2017). The shallow structure of a surface-rupturing fault in unconsolidated deposits from multi-scale electrical resistivity data: The 30 October 2016 M_w 6.5 central Italy earthquake case study. *Tectonophysics*, *717*(16), 628–644. https://doi.org/10.1016/j.tecto.2017.08.00
Vittori, E., Di Manna, P., Blumetti, A. M., Comerci, V., Guerrieri, L., Esposito, E., et al. (2011). Surface faulting of the 6 April 2009 M_w 6.3 L'Aquila earthquake in central Italy. *Bulletin of the Seismological Society of America*, *101*(4), 1507–1530. https://doi.org/10.1785/0120100140
Wallace, R. E. (1977). Profiles and ages of young fault scarps, north-central Nevada. *Geological Society of America*, *88-9*, 1267–1291.
Wallace, R. E. (1980). Degradation of the Hebgen Lake fault scarps of 1959. *Geology*, *8*, 225–229.
Wallace, R. E. (1984). Eyewitness account for surface faulting during the earthquake of 28 October 1983 Borah Peak, Idaho. *Bulletin of the Seismological Society of America*, *74*, 1091–1094.
Walsh, J. J., & Watterson, J. (1987). Distributions of cumulative displacement and seismic slip on a single normal fault surface. *Journal of Structural Geology*, *9*, 1039–1046.
Walters, R. J., Gregory, L. C., Wedmore, L. N. J., Craig, T. J., McCaffrey, K., Wilkinson, M., et al. (2018). Dual control of fault intersections on start-stop rupture in the 2016 Central Italy seismic sequence. *Earth and Planetary Science Letters*, *500*, 1–14. https://doi.org/10.1016/j.epsl.2018.07.043
Wesnousky, S. G. (2008). Displacement and geometrical characteristics of earthquake surface ruptures: Issues and implications for seismic-hazard analysis and the process of earthquake rupture. *Bulletin of the Seismological Society of America*, *98*(4), 1609–1632. https://doi.org/10.1785/0120070111
Westaway, R., & Jackson, J. (1984). Surface faulting in the southern Italy Campania-Basilicata earthquake of 23 November 1980. *Nature*, *312*, 436–438.
Westaway, R., & Jackson, J. (1987). The earthquake of 1980 November 23 in Campania–Basilicata (southern Italy). *Geophysical Journal of the Royal Astronomical Society*, *90*, 375–443. https://doi.org/10.1111/j.1365-246X.1987.tb00733.x
Wibberley, C. J., Yielding, G., & Di Toro, G. (2008). Recent advances in the understanding of fault zone internal structure: A review. In C. J. Wibberley, W. Kurz, J. Imber, R. E. Holdsworth, & C. Collettini (Eds.), *The internal structure of fault zone: Implications for mechanical and fluid-flow properties* (Vol. 299, pp. 5–33). London: Geological Society of London. https://doi.org/10.1144/SP299.2
Wilkinson, M. W., McCaffrey, K. J. W., Jones, R. R., Roberts, G. P., Holdsworth, R. E., Gregory, L. C., et al. (2017). Near-field fault slip of the 2016 Vettore M_w 6.6 earthquake (central Italy) measured using low-cost GNSS. *Scientific Reports*, *7*(1), 4612. https://doi.org/10.1038/s41598-017-04917-w
Witkind, I. J., Myers, B. W., Hadley, J. B., Hamilton, W., & Fraser, G. D. (1962). Geologic features of the earthquake at Hebgen Lake, Montana, August 17, 1959. *Bulletin of the Seismological Society of America*, *52*(2), 163–180.
Yamashita, T. (2009). Rupture dynamics on bimaterial faults and nonlinear off-fault damage. In E. Fukuyama (Ed.), *Fault-zone properties and earthquake rupture dynamics*, *International Geophysics Series* (Vol. 94, pp. 187–215). Amsterdam: Academic Press, Elsevier.
Yeats, R. S., Sieh, K., & Allen, C. R. (1997). *The geology of earthquakes*. New York and Oxford: Oxford University Press.